bioRχiv

Doublecortin regulates neuronal migration by editing the tubulin code

Muriel Sébastien,[1,2] Emily N. P. Prowse,[2] Adam G. Hendricks[2] and Gary J. Brouhard[1,*]
[1]Department of Biology, McGill University, Montréal, Québec, Canada
[2]Department of Bioengineering, McGill University, Montréal, Québec, Canada.
*Correspondence should be addressed to G.J.B. (gary.brouhard@mcgill.ca)

Doublecortin (DCX) is a neuronal microtubule-associated protein (MAP) that binds directly to microtubules via two Doublecortin (DC) domains. The DC domains sense the nucleotide state, longitudinal curvature, and protofilament number of the microtubule lattice, indicating a role in the regulation of microtubule structure in neurons. Mutations in DCX cause lissencephaly and subcortical band heterotopia (also known as double-cortex syndrome) due to impaired neuronal migration. To better understand the role of DCX in neuronal migration, we developed a model system based on induced pluripotent stem cells (iPSCs). We used CRISPR/Cas9 to knock out the *Dcx* gene in iPSCs and differentiated the cells into cortical neurons. Compared to control neurons, the DCX-KO neurons showed reduced velocities of nuclear movements. The reduced velocities correlated with an increase in the number of neurites early in the neuronal development process, consistent with a neuronal migration phenotype and previous findings in a DCX-KO mouse model. Neurite branching is regulated by a host of MAPs and other factors, as well as by microtubule polymerization dynamics. However, microtubule dynamics were unchanged in DCX-KO neurons, with similar growth rates, lifetimes, and numbers. Rather, we observe a significant reduction in tubulin polyglutamylation in DCX-KO neurons. Polyglutamylation is usually abundant in neurons and regulates microtubule severing enzymes and intracellular trafficking by molecular motors. Consistently, we observe that lysosomes in DCX-KO neurons show a reduction of their processivity. We propose that the reduction of polyglutamylation leads to increased neurite branching and thus reduced neuronal migration. Our results indicate an unexpected role for DCX in the homeostasis of the tubulin code.

Introduction

During human brain development, approximately 10^{10} newborn neurons migrate out of their stem cell niche to form the cerebral cortex (Herculano-Houzel 2009). Migrating neurons generally have two slender processes that extend from the cell body (Rakic 1972). Their migration can be divided into two steps: (1) elongation of the leading process and (2) translocation of the cell body in the direction of motion (Nadarajah & Parnavelas 2002). Both steps rely heavily on the neuronal microtubule cytoskeleton (Kapitein & Hoogenraad 2015). In the leading process, microtubules contribute pushing forces (Dogterom et al 2005), activate and reinforce actin polymerization, respond to guidance cues, and steer neuronal migration (Menon & Gupton 2016). In the cell body, microtubules and motor proteins generate forces that pull the nucleus forward (Umeshima et al 2007). And throughout the neuron, microtubules serve as roadways for the transport of organelles, synaptic vesicle precursors, and neurotrophic factors by motor proteins (Maday et al 2014).

To enable these diverse functions, the microtubule network is regulated and patterned at multiple levels. First, neurites have dynamic microtubules in their tips and stable microtubules in their shafts (Baas & Black 1990), which vary in their orientations (Baas et al 1988). Second, microtubules are altered by post-translational modifications (PTMs), known as the "tubulin code" (Magiera et al 2018, Roll-Mecak 2020, Verhey & Gaertig 2007), to create subpopulations of microtubules with variable chemical and mechanical properties. Third, the tubulin code governs a host of microtubule-associated proteins (MAPs), including structural MAPs (Bodakuntla et al 2019, Ramkumar et al 2018), polymerases and depolymerases (Howard & Hyman 2007), plus-end and minus-end regulators (Akhmanova & Steinmetz 2015), and motor proteins (Hirokawa et al 2009, Verhey & Ohi 2023). Each MAP has a specific localization, affinity, and function towards microtubules. Together, these regulatory mechanisms create complex microtubule "cartography" (Iwanski & Kapitein 2023), such as adjacent microtubule bundles that differ in their polarity and their PTMs (Tas et al 2017). Dysregulation of MAPs or loss of microtubule patterning can lead to brain malformation, neurodegeneration, and/or impaired neural function.

Doublecortin (DCX) is a MAP essential for human brain development (Francis et al 1999, Gleeson et al 1999). The *Dcx* gene is located on the X-chromosome and was discovered in 1998 in a cohort of patients with double cortex syndrome and X-linked lissencephaly (des Portes et al 1998, Gleeson et al 1998). These diseases are caused by mutations in DCX that lead to a failure in the radial migration of cortical neurons and result in a disorganized lamination of the cerebral cortex (Feng & Walsh 2001). How DCX mutations cause migration defects remains only partially understood, in part due to competing hypotheses about the structural role of DCX in microtubule regulation.

Most disease-causing mutations in DCX are missense mutations that cluster in a pair of tandem globular domains, known as the DC domains (Sapir et al 2000, Taylor et al 2000). DC domains bind to microtubules at the vertex of 4 tubulin dimers (Fourniol et al 2010, Moores et al 2004), a binding site shared with end-binding (EB) family proteins (Maurer et al 2012) and doublecortin-like kinase 1 (DCLK1)(Kim et al 2003, Omori et al 1998). The location of

this binding site makes DC domains (and EBs) highly responsive to the structural state of the microtubule lattice. The N-terminal domain, DC1, is tightly folded (Kim et al 2003) and binds to straight GDP lattices (Fourniol et al 2010). The second domain, DC2, is only partly folded (Burger et al 2016, Kim et al 2003) and binds GDP-Pi lattices (Manka & Moores 2018), curved lattices (Bechstedt et al 2014), and other tubulin intermediates (Manka & Moores 2020, Moores et al 2006). Together, the DC domains enable DCX to bind cooperatively to the microtubule lattice (Bechstedt & Brouhard 2012, Rafiei et al 2022). In addition, the DC domains bind in close proximity to kinesin motor domains on microtubules (Liu et al 2012) and impact kinesin-1 and dynein motility *in vitro* (Fu et al 2022, Monroy et al 2020). Many of these diverse structural interactions are disrupted by patient mutations in the DC domains (Bechstedt & Brouhard 2012, Bechstedt et al 2014, Manka & Moores 2020), suggesting a direct role for DCX in regulating microtubule structure and intracellular trafficking. Yet how mutations in DC domains disrupt function in the full context of the neuronal proteome remains unclear, especially at neurite tips and cell bodies where DCX is enriched (Friocourt et al 2003, Tint et al 2009).

Several *in vitro* and *in vivo* models have provided clues about the link between the disease phenotype seen in patients and the mechanistic behavior seen in reconstitution

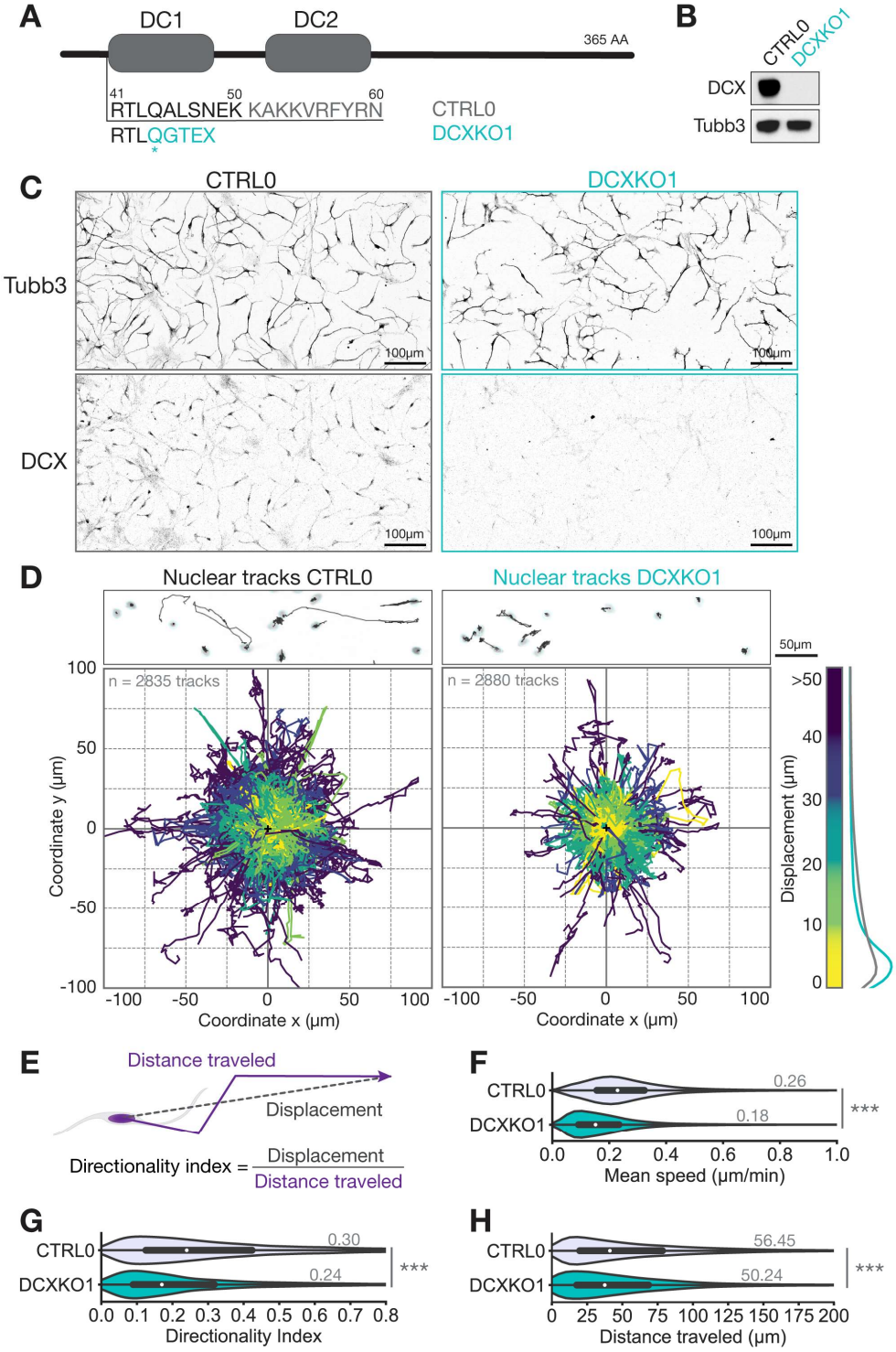

(Legend on next page)

assays. Surprisingly, *Dcx*$^{-/y}$ (hemizygote) mice have very mild phenotypes (Corbo et al 2002), with a cortical lamination indistinguishable from wildtype; only a double knock-out of DCX and DCLK1 gives rise to a disorganized cortex (Deuel et al 2006). Stronger phenotypes were observed with shRNA-mediated knock-down of DCX in rat embryos, which resulted in severe cortical migration defects (Bai et al 2003). This RNAi approach was shown to have significant off-target effects mediated by the miRNA *let7* (Baek et al 2014), complicating the interpretation of shRNA-mediated knock-down experiments e.g. (Liu et al 2012). However, explants of neurons from *Dcx*$^{-/y}$ mice allowed for an initial characterization of cortical neuron behavior: DCX knock-out disrupted the movement of the nucleus (nucleokinesis) and increased neurite branching (Kappeler et al 2006, Koizumi et al 2006). However, these phenotypes have not been linked to a clear mechanism of microtubule regulation. Basic cellular data on microtubules remains unmeasured, such as whether microtubule dynamics and intracellular trafficking are perturbed in neuronal models free of off-target effects.

To better understand DCX's role in neuronal migration, we took advantage of human induced pluripotent stem cells (iPSCs) and CRISPR/Cas9 gene editing. Human iPSC models have the following advantages: (1) human-specific genotypes, which are significant in the context of cortical development (Buchsbaum & Cappello 2019); (2) relatively simple knock-in of patient mutations in an isogenic background; and (3) direct observation of neurons immediately after terminal differentiation as opposed to harvesting of neurons from E18 rodent brains. Thus, we generated a series of DCX-KO and patient mutant iPSC models.

In our iPSC models, DCX-KO neurons showed impaired nucleokinesis and increased neurite branching, consistent with phenotypes in *Dcx*$^{-/y}$ rodent studies (Kappeler et al 2006, Koizumi et al 2006). We expand upon these studies by showing that the nucleokinesis defect is due to slow, meandering migration and that excessive branching is the result of higher rates of branch initiation. The processivity of lysosomes is impaired in DCX-KO neurons, linking DCX directly to intracellular trafficking. Taken together, these diverse phenotypes suggest a general dysregulation of the microtubule network. While searching for a common cause, we made the unexpected observation that DCX-KO neurons exhibit a significant reduction in tubulin polyglutamylation, one of the central PTMs of the neuronal tubulin code. We confirmed this reduction in 6 patient mutant knock-in neuronal lines. Expressing exogenous DCX in DCX-KO neurons was sufficient to rescue polyglutamylation levels back to control. Finally, we found that modulation of polyglutamylation levels could set the level of neurite branching. Overall, DCX expression increases tubulin polyglutamylation in neurons, indicating control of the tubulin code by a MAP. Thus, MAPs not only "read" the tubulin code but also "edit" it.

Results

Nuclear migration is impaired in DCX-KO cortical neurons

To understand the role of DCX in regulating the neuronal cytoskeleton, we used CRISPR/Cas9 genome editing to knock-out the expression of DCX in a male iPSC line. We designed a gRNA to target a sequence upstream of the first microtubule binding domain DC1, resulting in multiple iPSC clones expressing only N-terminal fragments (Fig. 1A and Fig. S1A-B). We confirmed DCX knock-out by Western blots and immunohistochemistry using antibodies against DCX's C-terminal domain (Fig. 1B-C and Fig. S1C). The morphology of our DCX-KO cells was indistinguishable from control cells at the iPSC stage as well as after induction to neural progenitor cells (NPCs). Terminal differentiation of DCX-KO NPCs into cortical neurons was confirmed by immunohistochemistry against β3-tubulin (Tubb3), a neuron-specific isotype (Fig. 1C and Fig. S1D). At DIV3 (3 days in terminal differentiation medium), iPSC-derived cortical neurons showed a bipolar morphology reminiscent of migrating neurons, with two or more slender processes that extended from the cell body (Nadarajah & Parnavelas 2002, Rakic 1972).

To determine if DCX-KO cortical neurons show phenotypes consistent with lissencephaly, we first measured the translocation of nuclei in control and DCX-KO cells using automated tracking algorithms (Fig. 1D-H, Fig. S2, and Videos S1-S2). Representative images of nuclei and their tracks are shown in Figure 1D (top panel), above 2-dimension plots of nuclear position (n ≅ 2800 tracks) over an 8 h observation window. These tracks showed a broad distribution of nuclear movements in all directions, independent of genotype. The distribution of displacements is large (distance between first and last coordinates, Fig. 1E), as some nuclei move significantly more than others of the same genotype. DCX-KO neurons have a greater proportion of small displacements (<10 µm) while control neurons have more large displacements (>10 µm) (Fig. 1D, right panel and Fig. S2C, right panel). To mitigate the effect of false-positive tracks from our algorithm, only tracks that

Figure 1: Nuclear migration is impaired in DCX-KO cortical neurons. (A) DCX contains two microtubule binding domains, DC1 and DC2. DCX-KO cells were obtained by indels introduced in Dcx's gene sequence before DC1. CTRL0 and DCXKO1 amino acid sequences are shown from residue 41 to 60. The asterisk shows the indel location and the resulting amino acid sequence in DCXKO1 is shown in cyan. **(B)** Immunoblot of CTRL0 and DCXKO1 neuron lysates at three days of differentiation (DIV3), with antibodies against Tubb3 and DCX. **(C)** CTRL0 and DCXKO1 neurons fixed and stained for Tubb3 and DCX at DIV3. **(D)** (top panel) Still images of live neurons with Syto nuclear dye. Nuclei that are detected by trackmate are circled in light blue, and their trajectories over the 8h period of imaging are shown in grey. (Bottom panel) Position plots showing a sample of trajectories extracted from CTRL0 (left) and DCXKO1 (right) nuclei tracking. All nuclei are considered to be at the same coordinates (0,0) at their first timepoint. Tracks are color-coded according to the displacement (distance between the first and the last position) of the nucleus. Distribution of displacement for both genotypes are shown on the right end side of the panel. *n*=2835 and 2880 nuclei respectively for CTRL0 and DCXKO1. **(E)** Schematics showing the displacement, distance traveled, and directionality index parameters. **(F)** Distribution of mean speed achieved by CTRL0 and DCXKO1 nuclei during the imaging period. **(G)** Distribution of directionality index or efficiency of the trajectory for CTRL0 and DCXKO1 nuclei. Higher directionality index indicates more unidirectional movement. **(H)** Distribution of distance traveled by CTRL0 and DCXKO1 nuclei during the imaging period. For F-H) White dots are showing median values, while the mean values are detailed on each plot. The thick black lines represent the quartiles. These three plots were cut-off to better show the main population, but the maximum values for distance traveled, mean speed and directionality index are 496.59 µm, 2.67 µm/min and 1 respectively. *n*=21826 CTRL0 tracks and 6461 DCX-KO tracks from 3 paired experiments, tracks with less than 30min of imaging time were excluded from the dataset. Statistical analysis was performed using the Kruskal-Wallis non parametric H test: *** $p<0.001$.

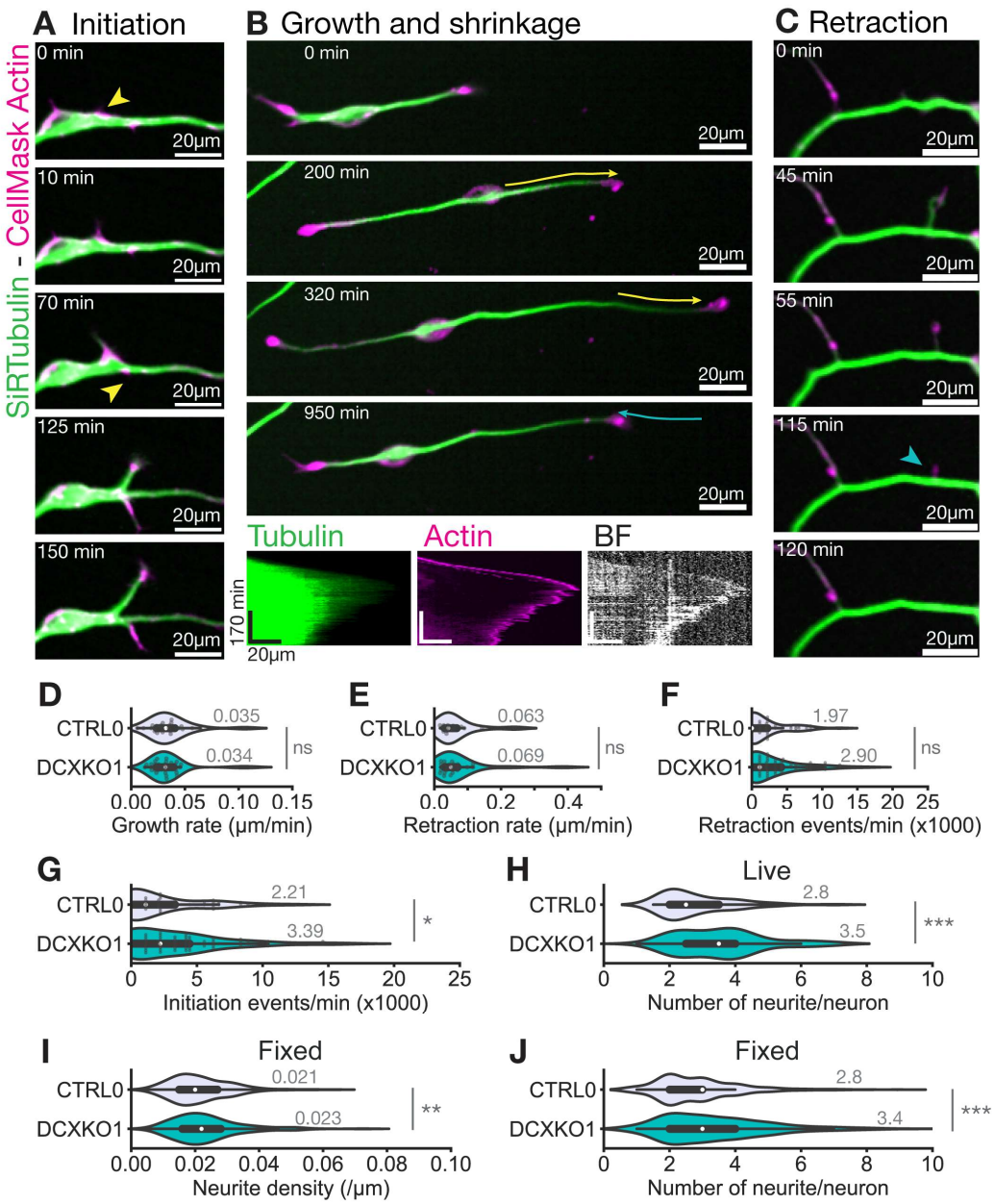

Figure 2: DCX-KO neurons establish more branches through increased rates of initiation/retraction. (A) (B) and **(C)** Representative images of a neurite initiation (A), growth/shrinkage (B) and retraction (C) events in a CTRL0 neuron recorded after incubation with tubulin and actin binding dyes: SiR-tubulin (green) and Cellmask actin (magenta). Yellow arrowheads show actin protrusions where a new neurite is initiated. cyan arrowheads show the remains of a neurite retracting completely. Yellow arrows show growth event and cyan arrows show retraction events. These events were used for calculation of growth and retraction speed (D and E), by measuring neurite length and lifetime on kymographs. An example kymograph is shown in the bottom panel in B with brightfield and fluorescence imaging. **(D)** Distribution of neurite growth rate in CTRL0 and DCXKO1 neurons. **(E)** Distribution of neurite retraction rate in CTRL0 and DCXKO1 neurons. For D-E, *n*=26 control and 38 DCX-KO events, from 2 independent experiments. Statistical analysis was performed using a Mann-Whitney U test: ns, nonsignificant. **(F)** Distribution of the number of neurite retraction events/min seen in CTRL0 and DCXKO1 neurons. Cells showing no retraction events were included in the analysis, but the points were not represented on the plot. **(G)** Distribution of the number of neurite initiation events/minute per neuron in CTRL0 and DCXKO1 neurons. Cells showing no initiation events were included in the analysis, but the points were not represented on the plot. **(H)** Number of neurites found per neuron in CTRL0 and DCXKO1 neurons. For F-H, *n*=68 control and 93 DCX-KO neurons from 2 independent experiments. Statistical analysis was performed using a Mann-Whitney U test: ns nonsignificant, * $p<0.05$, *** $p<0.001$. **(I)** Violin plot showing the distribution of neurite density per neuron for CTRL0 and DCXKO1 neurons in fixed samples. **(J)** Violin plot showing the distribution of neurite number per neuron for CTRL0 and DCXKO1 neurons in fixed samples. For I-J, *n*=323 control and 351 DCX-KO neurons from 3 independent experiments. Statistical analysis was performed using a Mann-Whitney U test: ** $p< 0.01$, *** $p<0.001$.

stayed visible for ≥6 frames (30 min) through the whole imaging period were analyzed (Fig. 1F-H and Fig. S2D-H). In control neurons, the nuclei had a mean speed of 0.260 ± 0.001 µm/min on average over the observation window (Fig. 1F). In contrast, in DCX-KO neurons, the nuclei had a significantly reduced speed of 0.186 ± 0.002 µm/min on average over the same window ($p<0.0001$, Fig. 1F). Moreover, we measured the maximum speed, or the fastest segment of each nucleus track (Fig. S2A). DCX-KO nuclei had reduced maximum speeds compared to control nuclei (DCX-KO 0.73 ± 0.01 µm/min vs. control 0.99 ± 0.01 µm/min, $p<0.0001$), suggesting a generalized decrease in speed as opposed to increased pausing. In parallel, we measured a "directionality index", which is the ratio between displacement and distance traveled, or the efficiency of the movement (Fig. 1E and 1H). A perfectly

straight trajectory would result in a directionality index of 1. The directionality index for both genotypes are relatively low as the direction of movement is random and not chemotactic or durotactic. However, DCX-KO neurons have a reduced directionality index compared to control (control 0.303 ± 0.001 vs DCX-KO 0.238 ± 0.003, $p<0.0001$), implying that they are 20% less efficient in their displacement relative to control neurons (Fig. 1G). This inefficiency causes DCX-KO cells to travel shorter distances (Fig. 1H, control 56.45 ± 0.35 µm vs DCX-KO 50.24 ± 0.59 µm, $p<0.0001$). We conclude that DCX-KO nuclei are slower, cover less distance, and are less directional, consistent with the nucleokinesis defects observed in *Dcx*$^{-/y}$ explant neurons (Belvindrah et al 2017, Kappeler et al 2006, Koizumi et al 2006).

DCX-KO neurons establish more branches through increased rates of initiation and retraction

Nucleokinesis is one of two steps in the process of neuronal migration; the other step is neurite extension (Coles & Bradke 2015, Dogterom & Koenderink 2019, Tsai & Gleeson 2005). DCX is enriched at neurite tips (Jean et al 2012, Tint et al 2009) (Fig. S4C), so we wondered if a defect in this compartment could also contribute to defects in neuronal migration. To test this idea, we imaged individual neurites, using either phase contrast microscopy or fluorescence microscopy with live cell fluorescent labels for microtubules and actin filaments (SiR-Tubulin and CellMask Actin, respectively). As shown in Fig. 2A-C (Videos S3-S5), we observed the canonical sequence of events (Kalil & Dent 2014, Pacheco & Gallo 2016): (A) first, neurites were initiated when a transient burst of actin polymerization was stabilized by microtubules; (B) the initiated neurite elongated at a relatively consistent velocity; (C) in most cases, the neurite later retracted. The balance of initiation and retraction events determines the net increase in neurite number per cell. We measured no significant change between control and DCX-KO cells in the rates of elongation or shrinkage (Fig. 2D-E); rather, only initiation and retraction events were affected. In DCX-KO neurons, the number of initiation events increased (Fig. 2G), as did the number of retraction events (Fig. 2F), resulting in an imbalance relative to controls. We measured a 2-fold increase in neurite formation (number of neurite initiations minus number of neurite retractions) per cell in DCX-KO neurons (Fig. 2H). We confirmed that DCX-KO increases neurite number using both types of live-cell imaging as well as direct counting of neurites in immunocytochemistry of fixed neurons (Fig. 2H and 2J). Figures 2D-H show the results from phase contrast microscopy to avoid any confounding effects of the fluorescent labels. To account for variations in cell developmental stage, we also measured the neurite density, or the number of neurites divided by the total length of the cell's neurites (Fig. 2I and Fig. S3) and found again a significant increase in DCX-KO neurons. We conclude that DCX plays a significant role in neurite formation (Bilimoria et al 2010, Kappeler et al 2006, Li et al 2014). Cortical neurons with an excessive number of neurites may struggle to migrate, because each branch pulls the cell body in a different direction (Chai et al 2015, Gupta et al 2003, Martini et al 2009). This hypothesis aligns with our previous observation of the nuclei being slower and showing wandering trajectories (Fig. 1D-H). Thus, we propose that the increase in branching in DCX-KO neurons contributes to the neuronal migration defects observed in patients with lissencephaly and double cortex syndrome.

Microtubule dynamics are unaffected in DCX-KO neurons

What could cause the increase in branching in DCX-KO neurons? Microtubules are well-known to be major players in both branching and neuronal migration (Cooper 2013, Dehmelt & Halpain 2004, Kawauchi & Hoshino 2008). DCX has been proposed to play a major role in the regulation of microtubule dynamics. In reconstitution assays with purified proteins, DCX promotes microtubule nucleation (Bechstedt & Brouhard 2012, Moores et al 2004), reduces the microtubule catastrophe frequency (Manka & Moores 2020), and slows their post-catastrophe shrinkage (Moores et al 2006). Hence, one plausible explanation for the branching phenotype is altered microtubule dynamics, whereby increased microtubule lifetimes/numbers would stabilize a greater percentage of the transient bursts of actin polymerization. As a first approach to look for changes in the microtubule cytoskeleton in DCX-KO neurons, we stained for α-tubulin and the neuronal specific β3-tubulin, as markers of the total microtubule population (Fig. 3A and S4A-B). We found that DCX-KO neurons have equivalent levels of total tubulin, albeit with a slight reduction in the intensity of β3-tubulin.

Then we looked specifically for changes in microtubule dynamics. We observed dynamic microtubules by transient expression of the end-binding protein EB3-mCherry in DCX-KO neurons (Fig. 3B and videos S6-S7). Since DCX is enriched in neurite tips (growth cones) (Jean et al 2012, Tint et al 2009) (Fig. S4C), we measured neurite tips and shafts separately. However, regardless of region, we found no significant differences in microtubule dynamics between control and DCX-KO (Fig. 3C-D and Fig. S5), including in the densities of EB3 comets (0.40 ± 0.04 µm^{-2} control vs 0.44 ± 0.04 µm^{-2} DCXKO1, $p=0.43$), their velocities (10.51 ± 0.34 µm/min control vs 9.97 ± 0.38 µm/min DCXKO1, $p=0.24$), and lifetimes (GC: 13.08 ± 0.46 s control vs 12.46 ± 0.57 s DCXKO1, $p=0.18$). The characteristics of dynamic microtubules in our iPSC-derived neurons were equivalent to what was found in other studies (Dema et al 2023, Lindhout et al 2020). We did observe a slight increase in the proportion of retrograde comets specifically, suggesting a role for DCX in the orientation of growing microtubules (Fig. 3E and Fig. S5E), consistent with recent cryo-electron tomography of microtubules in *Dcx*$^{-/y}$ mouse neurons (Atherton et al 2022). We also noticed that the area covered by EB3 carrying microtubules was reduced in DCX-KO neurites, indicating that DCX may contribute to growth cone morphology (Fig. S5C). However, we conclude that DCX does not regulate microtubule dynamics in our model. Rather, other factors determine the growth rates, lifetimes, and nucleation rates in neurons. An important caveat of our results is that we cannot measure the rate of post-catastrophe shrinkage, which DCX does change *in vitro*, because EBs dissociate from shrinking ends. However, given that all other dynamic instability parameters are unchanged, it is unlikely that shrinkage rates are affected.

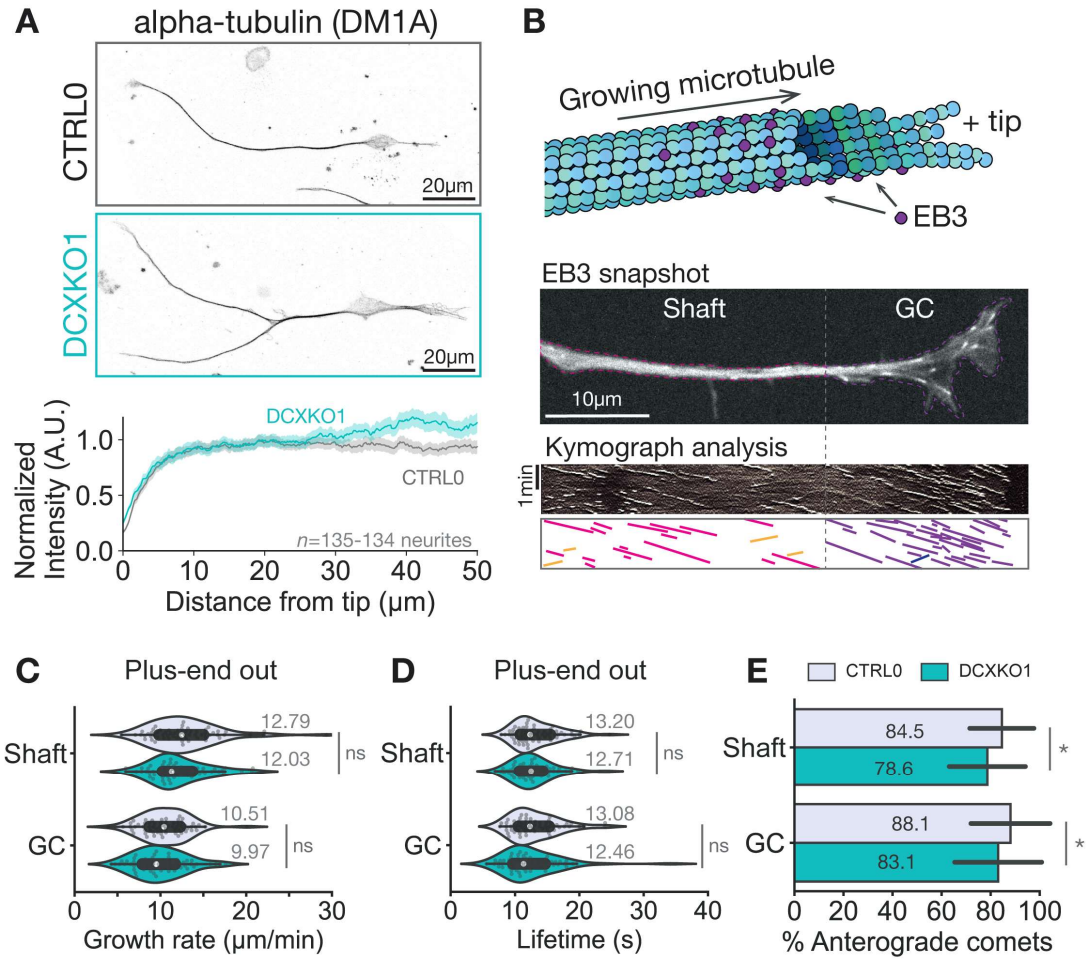

Figure 3: Microtubule dynamics are unaffected in DCX-KO neurons. (A) (Top) Immunostaining of CTRL0 and DCXKO1 neurons at DIV3 with a Tubulin-β3 specific antibody, and (Bottom) mean intensity profile found in the distal tip of neurons from both genotypes, SEM are shown in lighter grey (CTRL0) and lighter cyan (DCXKO1). Images included in the analysis are from *n*=135 CTRL0 neurites and *n*=134 DCXKO1 neurites from 3 experiments. Statistical analysis was performed using the Mann-Whitney non parametric U test: * $p<0.05$. **(B)** Schematics of the experimental procedure and analysis method for measuring microtubule dynamics. NPCs are electroporated with the plus-tip marker EB3-mCherry, and neurons are imaged at DIV3. Each comet is assigned to a domain (Shaft or growth cone (GC)), and its characteristics are measured: length, lifetime, growth rate, and direction. **(C)** Violin plot showing the distribution of growth rates for plus end out comets in shaft or growth cone of CTRL0 and DCXKO1 neurons. **(D)** Violin plot showing the distribution of lifetimes for plus end out comets in shaft or growth cone of CTRL0 and DCXKO1 neurons. **(E)** Box plot showing the proportion of plus end out comets in the shaft and growth cone of CTRL0 and DCXKO1 neurons. For C-E, *n*=63 CTRL0 and *n*=63 DCXKO cells from 4 experiments. Statistical analysis was performed using the Mann-Whitney non parametric U test: ns nonsignificant, * $p<0.05$.

DCX-KO neurons show altered DCLK1 localization and lysosome motility

DCX has also been proposed to play a role in regulating intracellular trafficking. Stable microtubules are necessary for intracellular trafficking by kinesins and dynein, and DCX directly regulates the motility of motor proteins in vitro (Fu et al 2022, Liu et al 2012, Monroy et al 2020). However, there is some ambiguity between observations *in vitro* and in cells. DCX reduces the landing rate and run length of kinesin-1 motors *in vitro* but not kinesin-3 motors (Monroy et al 2020), while in neurons, DCX shRNA caused reduced run lengths of kinesin-3 cargos (Liu et al 2012). In addition, DCX binds directly to dynein complexes and negatively regulates retrograde transport (Fu et al 2022). The absence of DCX might also modify the localization or behavior of other MAPs involved in the regulation of trafficking, such as Tau (Chaudhary et al 2018, Monroy et al 2018), MAP2 (Gumy et al 2017), DCLK1 (Lipka et al 2016), and others (Bodakuntla et al 2019, Ramkumar et al 2018, Siahaan et al 2022). As an example of this competition, DCX and Tau were shown to bind the microtubule lattice in a mutually exclusive manner in non-neuronal cell lines and in rat neurons (Ettinger et al 2016, Tint et al 2009).

To determine how intracellular trafficking may be directly or indirectly impacted by DCX-KO, we measured the intensity profile of several molecular motors and MAPs in control and DCX-KO neurons by immunocytochemistry (Fig. 4A-B). To maximize signal, we did not use detergent to extract the cytoplasmic pool of proteins (See methods), meaning we detect both bound and unbound proteins. The intensity of polarity markers MAP2 and Tau did not change in DCX-KO neurons, perhaps because they are not strongly expressed in neurons at this early pre-polarization stage (Lindhout et al 2020). We found an increased signal by 1.4-fold for DCLK1 in DCX-KO neurons (Fig. 4A), which was not associated with higher expression levels (Fig. S6B). DCLK1 is enriched in the distal tip of neurites (Fig. S6A), suggesting a partial rescue of DCX's absence by its homologue (Deuel et al 2006, Tanaka et al 2006). Kinesin-1, kinesin-2, kinesin-3 and dynein intensities were not significantly modified in DCX-KO neurons (Fig. 4A). However, the lack of change in

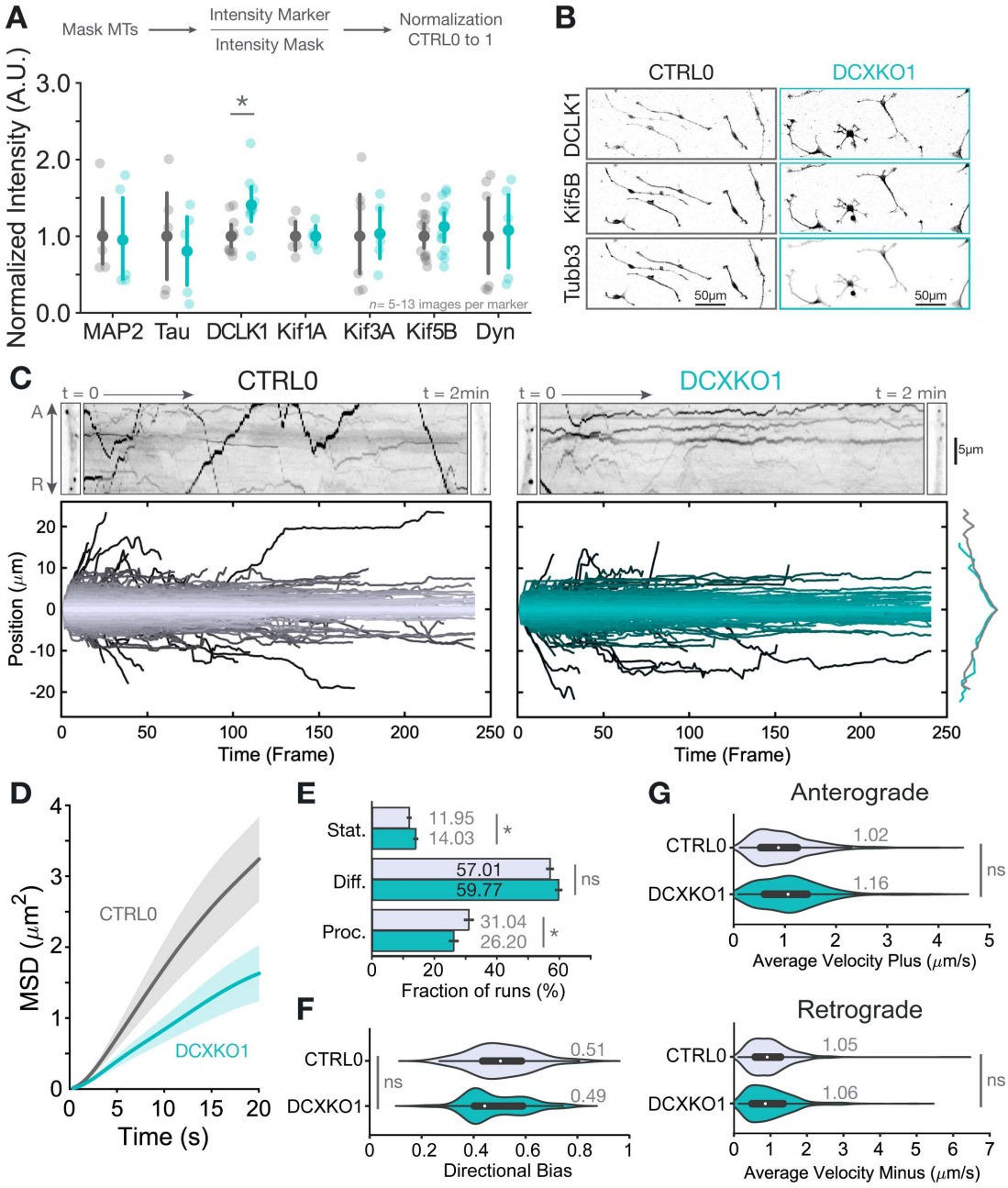

Figure 4: DCX-KO neurons show altered DCLK1 localization and lysosome motility. (A) Compared mean intensity for MAP2, Tau, DCLK1, Kif1A, Kif3A, Kif5B, and Dynein in CTRL0 or DCXKO1 DIV3 immuno-stained neurons. The analysis pipeline is shown above the plot: a mask of the microtubules (MTs) was made, and the intensity of the marker was normalized to the intensity of the mask and to the control condition. Each transparent point represents a single image, while the opaque points show mean values, error bars represent the confidence intervals. Analyses are from *n*=5-13 CTRL0 or DCXKO1 images from 2-4 experiments. Statistical analysis was performed using the Mann-Whitney non parametric U test: * $p<0.05$. **(B)** Representative images from CTRL0 and DCXKO1 DIV3 neurons stained for DCLK1, Kif5B and Tubb3. **(C)** (Top) Representative still images of CTRL0 and DCXKO1 straight neurite sections after incubation with the Lysotracker® dye, and 2min kymographs of those same sections. A means anterograde, and R retrograde. (Bottom) Position plots for lysosomes detected using Trackmate during the 241 frames for CTRL0 and DCXKO1 neurons. The distribution of these positions was also plot and is represented on the right end side of the position plots. **(D)** Mean squared displacement (MSD) of lysosomes inside CTRL0 and DCXKO1 neurites. **(E)** Proportion of tracked cargos that are either stationary (Stat.), Diffusive (Diff.) or Processive (Proc.). **(F)** Directional bias of lysosome cargos in CTRL0 and DCXKO1 neurons, where 0 corresponds to retrograde only and 1 corresponds to anterograde only. **(G)** Violin plots of the average velocity for anterograde (plus-ended) displacement and retrograde (minus-ended) displacement of lysotracker® cargos in CTRL0 and DCXKO1 DIV3 neurons. All trajectories (6082 for control and 3887 for DCXKO1) were obtained from *n*=41 control and 30 DCXKO1 neurons from 3 independent experiments. Statistical analysis was performed using the Student's t-test: ns nonsignificant, * $p<0.05$.

motor localization (Fig. S6A) does not exclude a defect in intracellular trafficking.

To test the role of DCX in regulating cargo trafficking, we measured the trajectories of lysosomes using the pH-sensitive Lysotracker® dye (Videos S8-S9). Lysosomes move in a bidirectional manner using kinesin-1, kinesin-2, kinesin-3 and dynein motors, making them an excellent cargo to assess broad trends in intracellular trafficking (Bentley et al 2015, Pu et al 2016). Figure 4C shows Lysotracker kymographs and extracted trajectories for control and DCX-KO neurons. In both cases, we observed bidirectional transport with similar distributions of trajectories (right panel). We characterized this transport further by measuring the mean-squared displacement

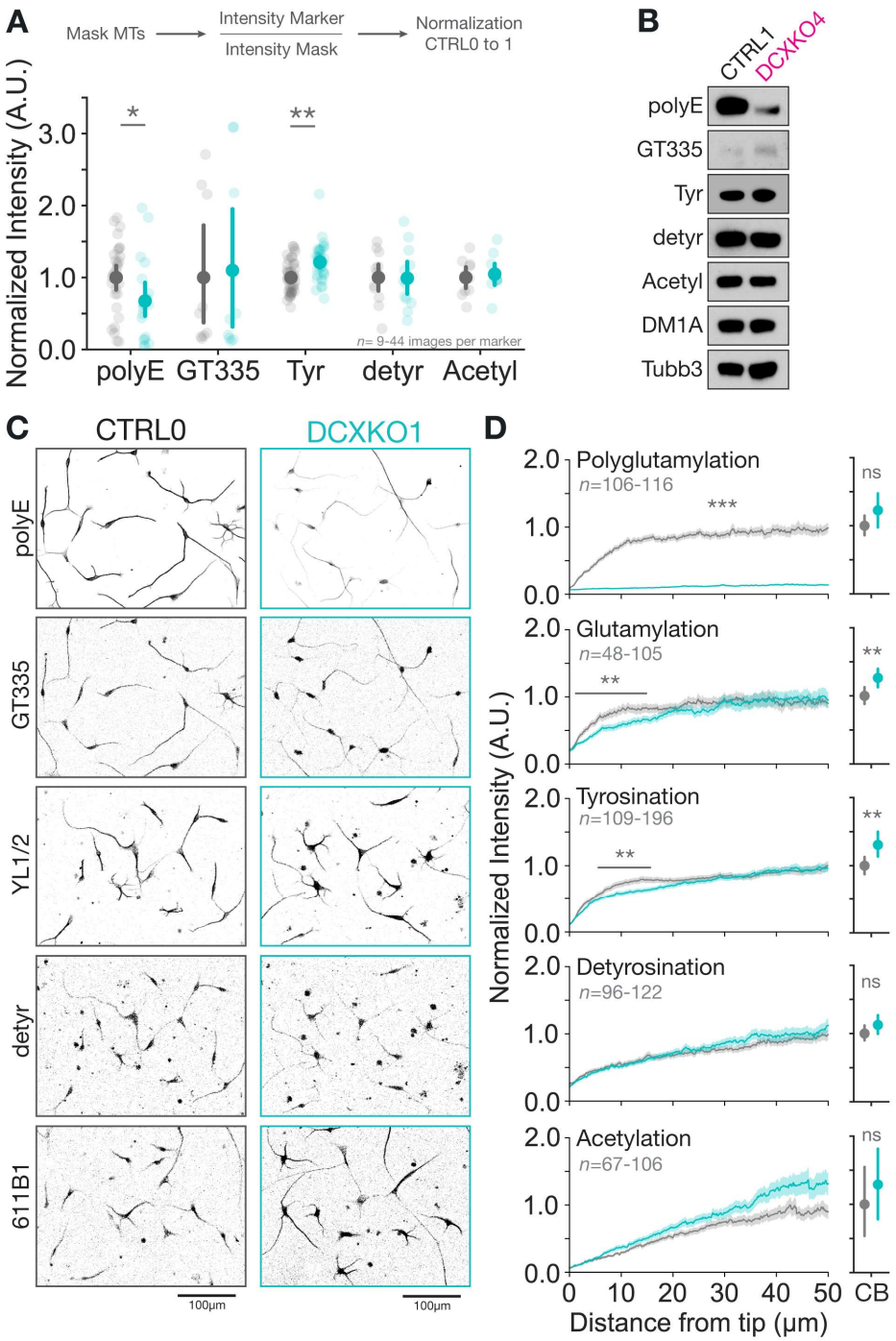

Figure 5: DCX-KO disrupts microtubule polyglutamylation. (A) Compared mean intensity for polyglutamylation (polyE), glutamylation (GT335), tyrosination (Tyr), detyrosination (detyr), and acetylation (Acetyl) in CTRL0 or DCXKO1 DIV3 immunostained neurons. The analysis pipeline is shown above the plot: a mask of the microtubules (MTs) was made, and the intensity of the marker was normalized to the intensity of the mask and to the control condition. Each transparent point represents a single image, while the opaque points show mean values, error bars represent the confidence intervals. Plots are from *n*=9-44 CTRL0 or DCXKO1 images from 3-6 experiments. Statistical analysis was performed using the Mann-Whitney non parametric U test: * $p<0.05$, ** $p<0.01$. **(B)** Immunoblot showing the relative post-translational modifications levels in CTRL1 and DCXKO4 DIV3 neurons. **(C)** Representative images of CTRL0 and DCXKO1 neurons stained for PTMs with the following antibodies: polyE, GT335, YL1/2, detyr, 611B1. **(D)** Intensity profiles for the PTMs levels in distal neurites and cell bodies (CB) of CTRL0 and DCXKO1 DIV3 neurons. Error bars represent the confidence interval. Plots are from *n*=48-196 CTRL0 or DCXKO1 neurites and *n*=23-90 cell bodies, from at least 3 experiments. Statistical analysis was performed using the Mann-Whitney non parametric U test: ns nonsignificant, * $p<0.05$, ** $p<0.01$, *** $p<0.001$.

(MSD) of lysosome position, radius of gyration (Rg), directional bias, and velocities as a function of time (Fig. 4D-G and S7). The Rg, MSD and extracted α value which assess general motility of cargos are significantly decreased in DCX-KO neurons (Fig. 4D and Fig. S7A-B), confirming the impact of the KO on intracellular trafficking. All the trajectories used for MSD assessment can be sorted as stationary, diffusive or processive depending on their characteristics (Fig. 4E, see Methods). Interestingly, the proportion of processive motility is significantly reduced in DCX-KO neurons (control 31.04 ± 1.35 % vs DCX-KO 26.20 ± 1.32 %, p=0.012, *) and correspondingly the fraction of diffusive (control 57.01 ± 1.03 % vs DCX-KO 59,77 ± 0.95 %, p=0.053, ns) and stationary motility increased (control

11,95 ± 0.53 % vs DCX-KO 14,03 ± 0.58 %, p=0.010, *). We noticed that lysosomes in DCX-KO neurons are more unidirectional than in control cells, as indicated by a bimodal directional bias (Fig. 4F). However, lysosome velocity was not affected in either the minus- or plus-end direction (Fig. 4G). Altogether, in DCX-KO neurons, lysosomes are less processive. Importantly, this trafficking defect is mild and possibly insufficient to explain the phenotypes found in DCX-KO neurons (Fig. 2).

Thus far, analysis of our DCX-KO neurons has revealed complex and pleiotropic phenotypes, namely a slowed nucleokinesis, increased rate of branch initiation, increased proportion of misoriented microtubules, and reduction in lysosome processivity. These disparate phenotypes point to an upstream regulator of microtubule physiology: something which, if dysregulated, disrupts microtubule homeostasis at many levels. We hypothesized that this upstream regulator could be the tubulin code.

DCX-KO disrupts microtubule polyglutamylation

The tubulin code is an information system for microtubule specialization that contributes to the processivity of motor proteins (Sirajuddin et al 2014, Tas et al 2017), binding affinity of MAPs (Bonnet et al 2001, Boucher et al 1994), and microtubule spacing and geometry (Cueva et al 2012). For example, acetylated microtubules (Acetyl) are more flexible and predominantly bundled (Balabanian et al 2017, Portran et al 2017, Tas et al 2017). Recently, acetylation has been linked to neurite branching in a model a tubulinopathy (Hoff et al 2022). Tyrosinated microtubules (Tyr) act as preferred tracks for kinesins 3 and 5 (Lessard et al 2019, Sirajuddin et al 2014) and dynein (McKenney et al 2016, Tas et al 2017); Polyglutamylation (polyE) and detyrosination (detyr) regulate MCAK and severing enzymes binding, that are responsible for modified branching patterns when depleted (Homma et al 2003, Valenstein & Roll-Mecak 2016), reviewed in (Janke & Magiera 2020, Moutin et al 2021). Therefore, we wondered if the tubulin code could be altered in DCX-KO neurons.

To test for changes in the tubulin code, we performed immunocytochemistry and Western blots in control and DCX-KO neurons, with antibodies against acetylation (611B1), tyrosination (YL1/2), detyrosination (detyr), initial glutamylation (GT335) and polyglutamylation (polyE) where glutamate side chains are reversibly added to the C-terminal tails of α- and β-tubulin (Audebert et al 1993, Redeker et al 1992). (Fig. 5A-B and S8). GT335 recognizes all glutamate chains through the initial residue, while polyE detects glutamate chains of 4 residues or more (Lacroix et al 2010, Wolff et al 1992). Remarkably, we observed a dramatic reduction specifically in tubulin polyglutamylation by both Western blot and immuno-cytochemistry (polyE – Fig. 5A-B and Fig. S8). In addition, detection of all glutamate chains with GT335 in Western blots is mildly increased in DCX-KO neurons. We analyzed the subcellular distribution of staining in neurites and cell bodies (CB) and confirmed an increase in initial glutamylation specific to cell bodies and a drastic reduction in polyglutamylation only in neurites (Fig. 5C-D). In parallel, we observed that acetylation and detyrosination levels, which label long-lived microtubules, were unchanged in DCX-KO neurons compared to control, while tyrosination is mildly increased in cell bodies. These results indicate that DCX can directly or indirectly regulate the tubulin code, especially polyglutamylation levels in neurites.

DCX reduces neurite numbers by increasing tubulin polyglutamylation levels

We found that DCX may play a role in regulating the tubulin code, but we wondered if these changes in PTM levels could result in the branching phenotype we have seen in DCX-KO neurons. To link DCX and polyglutamylation, we tested whether the expression of DCX could rescue polyglutamylation levels and the branching phenotype in DCX-KO neurons. We electroporated a DCX-GFP construct in control and DCX-KO neurons and measured both the polyglutamylation (polyE) levels and neurite density (Fig. 6A-C and Fig. S9A-D). In DCX-KO neurons we found that with the expression of DCX-GFP, polyglutamylation levels were increased and branch density was accordingly reduced to match those found in control neurons. Surprisingly, the overexpression of DCX-GFP in control neurons reduced polyglutamylation levels and increased neurite density, similar to DCX-KO neurons (Fig. 6B-C). This result is consisent with overexpression experiments done in mouse models, which also led to an increase in neurites (Cohen et al 2008, Yap et al 2016). Moreover, the data suggest that the effects of DCX protein concentrations are biphasic, with an intermediate protein concentration achieving normal polyglutamylation levels and neurite densities. To further address the link between polyglutamylation and neurite density, we treated cells with taxol, a well-known chemotherapy drug, that stabilizes microtubules (Yang & Horwitz 2017). Low doses of Taxol were previously shown to increase detyrosination, acetylation and poly-glutamylation (Hammond et al 2010). We therefore applied taxol for 48h at 100nM to neurons and measured their polyglutamylation levels and neurite density (Fig. 6D-F and Fig. S9E-F). Neurons treated with taxol showed an increase in polyglutamylation levels in their branches independently of their genotype (Fig. 6E). Polyglutamylation was increased by ~1.2-fold in control cells and by 1.6-fold in DCX-KO cells. In parallel to these changes in polyglutamylation levels, neurite density decreased by about 20% in taxol-treated cells (Fig. 6F) indicating a correlation between polyglutamylation levels and neurite number. Therefore, we can conclude that DCX restricts neurite numbers by increasing polyglutamylation levels in our iPSC model.

DCX patient-mutant neurons have reduced polyglutamylation levels

To test the relevance of our findings in the context of disease, we used a CRISPR/Cas9 approach to introduce lissencephaly-causing patient mutations to DCX in iPSCs. We used previously characterized missense mutations located in both domains of DCX: S47R, Y64N, D86H in DC1 and R178L, P191R, and R192W in DC2 (Bahi-Buisson et al 2013, Bechstedt et al 2014, Leger et al 2008). We assessed polyglutamylation levels in iPSC-derived neurons from these patient mutations by Western blot and immunocytochemistry (Fig. 7A-B). Remarkably, both methods showed reduced polyglutamylation levels in all the patient mutations independently of the mutation locus.

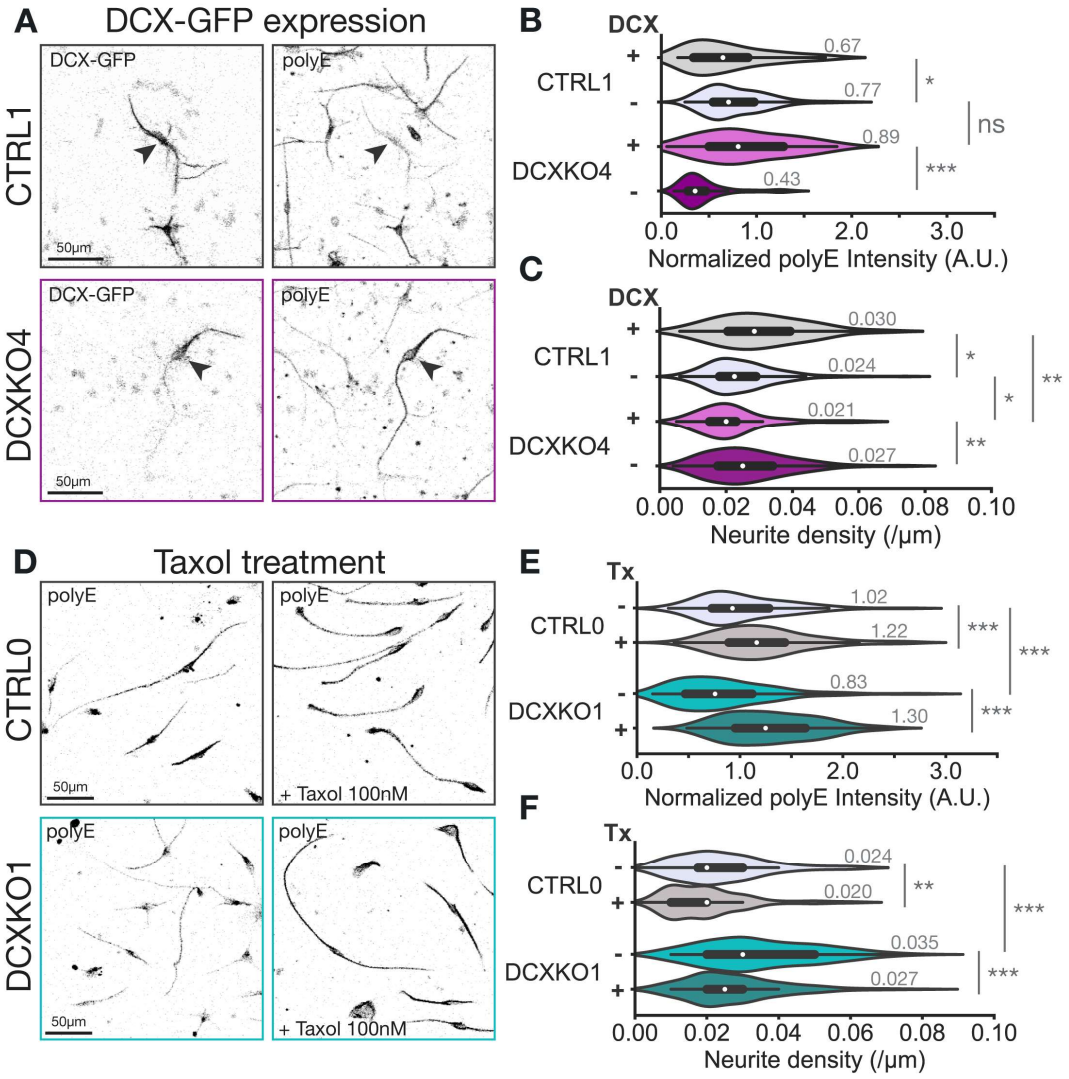

Figure 6: DCX reduces neurite numbers by increasing tubulin polyglutamylation levels. (A) Representative images of CTRL1 and DCXKO4 DIV3 neurons electroporated with DCX-GFP and stained for polyglutamylation. The arrowheads are showing the same cell in both channels (GFP, and polyE). **(B)** Violin plots showing the polyglutamylation (polyE) intensity in CTRL1 and DCXKO4 DIV3 neurons with or without DCX-GFP electroporation. **(C)** Violin plot showing the neurite density in CTRL1 and DCXKO4 DIV3 neurons with or without DCX-GFP electroporation. For B-C, images included in the analysis are from *n*=178 CTRL1, 34 CTRL1+DCX-GFP, 171 DCXKO4 and 45 DCXKO4+DCX-GFP neurons from 3 experiments. Statistical analysis was performed using the Mann-Whitney non parametric U test: ns nonsignificant, * p<0.05, ** p<0.01, *** p<0.001. **(D)** Representative images of CTRL0 and DCXKO1 DIV3 neurons stained for polyglutamylation (polyE) after 48h in regular media or 48h in media supplemented with 100nM taxol. **(E)** Violin plots showing the polyglutamylation (polyE) intensity in CTRL0 and DCXKO1 DIV3 neurons with or without treatment with taxol. **(F)** Violin plots showing the neurite density in CTRL0 and DCXKO1 DIV3 neurons with or without treatment with taxol. For E-F, images included in the analysis are from *n*=84 CTRL0, 120 CTRL0+taxol, 172 DCXKO1 and 160 DCXKO1+taxol neurons from 2 experiments. Statistical analysis was performed using the Mann-Whitney non parametric U test: ns nonsignificant, ** *p*<0.01, *** *p*<0.001.

Overall, our findings validated the notion of DCX regulating polyglutamylation levels and therefore MAP affinity and microtubule organization. Moreover, these results corroborate the necessity of proper tubulin code regulation in development of the cerebral cortex, to avoid neuronal migration defects like lissencephaly and subcortical band heterotopia.

Discussion

In summary, the iPSC models we developed show how DCX regulates the tubulin code to control neuronal migration, providing insight into the cellular basis of double-cortex syndrome and X-linked lissencephaly. DCX-KO neurons showed pleiotropic defects, including meandering nucleokinesis (Fig. 1), excessive branch initiation (Fig. 2), and less directed lysosome trafficking (Fig. 4), but without changes in microtubule dynamics (Fig. 3). These defects can be explained by a strong reduction in polyglutamylation levels (Fig. 5), an unexpected finding that we confirmed in 6 patient-mutant iPSC models (Fig. 7), suggesting that misregulation of the tubulin code contributes to the disease state. Both polyglutamylation levels and branch density were rescued by DCX expression as well as by taxol treatment (Fig. 6), indicating a robust correlation between polyglutamylation and neuronal morphology.

Polyglutamylation is a complex, reversible, and heterogenous feature of neuronal microtubules. A family of 9 glutamylases (TTLLs) (Janke et al 2005, van Dijk et al 2007) competes against a family of 6 deglutamylases (CCPs) (Rogowski et al 2010) to create glutamate chains of variable length and structure (Janke & Magiera 2020). The members of each family have specialized roles, such as branch initiation (e.g., TTLL4) versus elongation (e.g., TTLL6)

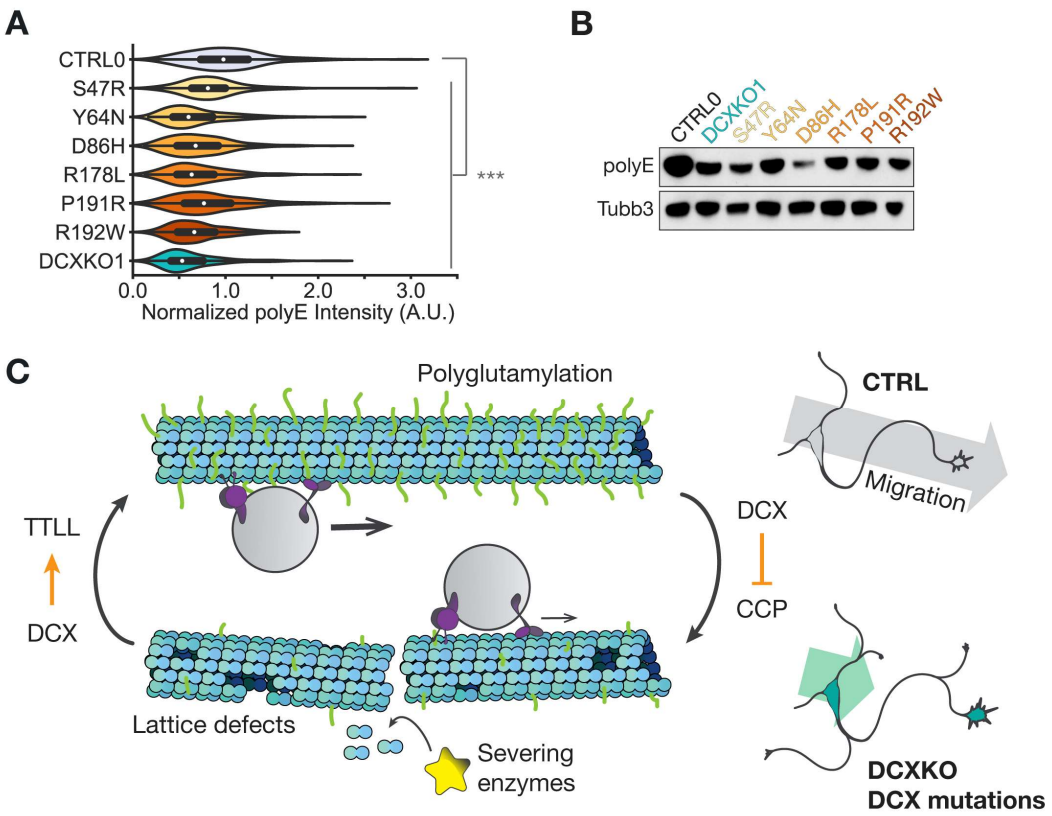

Figure 7: Model of a feedback regulation of the tubulin code by the MAP DCX. (A) Violin plots showing the polyglutamylation (polyE) intensity in stained DIV3 neurons carrying the following DCX patient mutations: S47R, Y64N, D86H, R178L, P191R, R192W, and compared to CTRL0 and DCXKO1. Images included in the analysis are from *n*= 384 CTRL0, 314 D86H, 177 DCXKO1, 323 P191R, 260 R178L, 287 R192W, 215 S47R, 289 Y64N neurons from 3 experiments. Statistical analysis was performed using the Mann-Whitney non-parametric U test: *** $p<0.001$. **(B)** Immunoblot showing polyglutamylation levels in CTRL0, DCXKO1 and mutant DIV3 neurons (DC1: S47R, Y64N, D86H, DC2: R178L, P191R, R192W). **(C)** Control neurons have high polyglutamylation levels. In this context, DCX inhibits CCPs or activate TTLLs leading to two molecular phenotypes in DCX-KO neurons: a decrease in polyglutamylation of the microtubule lattice and an impeded cargo motility. The addition or association of these two mechanisms result in an excessive production of neurite and a decrease in migration speed and efficacy in DCX-KO and mutated neurons.

(Mahalingan et al 2020), or shortening (e.g., CCP1) versus branch removal (CCP5) (Rogowski et al 2010). Additionally, α-tubulin and β-tubulin polyglutamylation are distinct (Alexander et al 1991, Bodakuntla et al 2021, Edde et al 1990). Excessive polyglutamylation upon loss of CCP activity causes neurodegeneration (Magiera et al 2018, Shashi et al 2018), while our results link reduced polyglutamylation to a neuronal migration disease. Thus, the competition between glutamylases and deglutamylases must be regulated to produce the patterns of polyglutamylation essential for neuronal health.

We can imagine two mechanisms by which DCX could regulate glutamylases and/or deglutamylases (Fig. 7). First, DCX could directly bind the enzymes, e.g. to bring a glutamylase to the microtubule lattice or to hold a deglutamylase at bay. For example, DCX could recruit the conserved cationic microtubule-binding domain of TTLLs (Garnham et al 2015). Alternatively, DCX could indirectly affect the enzymes by changing the structural configuration(s) of tubulin's C-terminal tails, namely by altering the enzymes' substrate. We currently favor an indirect model, given DCX's sensitivity to structural features such as lattice curvature (Bechstedt et al 2014), nucleotide state (Manka & Moores 2018), and protofilament number (Bechstedt & Brouhard 2012, Moores et al 2004), but time will tell. Either model needs to explain why long glutamate chains are reduced only in neurites, while short chains are barely affected (Fig. 5D), which suggests specific regulation of "elongases" (Mahalingan et al 2020) or their reverse enzymes. Further, we must explain why polyglutamylation is reduced by DCX-KO *and* overexpression (Fig. 6B). For example, overloading the lattice with DCX could impede the glutamylation reaction. Much remains unknown, and what is needed is a comprehensive understanding of DCX, the glutamylases, and the deglutamylases, including their expression patterns, localization(s), regulatory mechanisms, and impacts on neuronal morphology.

Our observation of a correlation between polyglutamylation and branching morphology (Fig. 6) harmonizes with many recently-discovered links between the tubulin code and proteins involved in branching pathways (Kalil & Dent 2014). Several MAPs play a role in branching, such as the severing enzymes spastin and katanin (Yu et al 2008). Severing enzymes were proposed to fragment the microtubule network (Roll-Mecak & Vale 2006); notably at branch points, as proliferation of short microtubules might stabilize transient actin protrusions (Yu et al 2008). It is important to note that these proposals predate the discovery of microtubule self-repair (Schaedel et al 2015), which counteracts severing damage and "refreshes" the lattice (Vemu et al 2018); such that severing enzymes might act to repair and strengthen microtubules rather than fragment them. In any case, the damage rate of these enzymes is biphasic with respect to

polyglutamylation: the rate first increases as glutamate chains get longer but then decreases beyond some optimal chain length *in vitro* (Lacroix et al 2010, Valenstein & Roll-Mecak 2016). A link between microtubule damage and DCX is hinted at by cryo-electron tomography of microtubules in *Dcx*$^{-/y}$ mouse neurons. The number of large lattice defects increased relative to control (Atherton et al 2022). To further complicate the picture, severing enzymes are inhibited by structural MAPs such as tau (Siahaan et al 2022, Tan et al 2019), and tau's affinity for microtubules is increased by polyglutamylation (Genova et al 2023). Spastin and tau are not alone, especially once intracellular trafficking is considered (see below). The dynamics of this complex system may require computational or analytical modeling. In our experiments, we observed a primarily negative correlation between polyglutamylation and branch density, but positive correlations have been observed in other conditions (Gallo & Letourneau 1999).

Changes in polyglutamylation levels impact motor proteins (Hammond et al 2010, Sirajuddin et al 2014), but DCX also regulates motor proteins directly, potentially having differential effects. In reconstitution assays, kinesin-1 has a reduced run length on polyglutamylated microtubules (Genova et al 2023), and DCX-coated microtubules reduce kinesin-1's landing rate (Monroy et al 2020). Similarly, the run length of kinesin-3 is increased on polyglutamylated microtubules (Lessard et al 2019), while DCX-coated microtubules do not affect kinesin-3 motility *in vitro* (Monroy et al 2020). Both kinesin-1 and kinesin-3 are present on lysosomes (Guardia et al 2016), and our results indicate that DCX-KO primarily affects the fraction of lysosomes which are stationary versus processive. Other cargos regulated by DCX-family proteins are synaptophysin (Deuel et al 2006), Vamp2 (Liu et al 2012), dense-core vesicles (Lipka et al 2016), and TrkB (Fu et al 2022). The phenotypes of disrupted intracellular trafficking will need to be explained in light of both direct interactions between DCX and motor proteins (Fu et al 2022, Liu et al 2012) as well as changes in polyglutamylation, and polyglutamylation's effects on affinity of the other MAPs like tau (Genova et al 2023) (Fig. 7).

Our study did not address a potential role for DCX in the regulation of the actin cytoskeleton. The data on DCX and actin are mixed. DCX has been proposed to modulate actin through interactions with spinophilin, an actin-binding protein (Bielas et al 2007). *Dcx*$^{-/y}$ neurons showed reduced actin staining in some experiments (Fu et al 2013), but this result was not reproduced in recent cryo-ET (Atherton et al 2022); if anything, our DCX-KO neurons show increased actin staining (Fig. S4). In any case, our results on polyglutamylation do not exclude a link between DCX and actin. Indeed, given the complexity of MT-actin crosstalk (Dogterom & Koenderink 2019), it's likely that the tubulin code impacts the actin cytoskeleton as well. We look forward to exploring these links in the future.

Sadly for us, our results argue against a role for DCX in the regulation of microtubule dynamics, which we and others had speculated based on DCX's potent nucleation and anti-catastrophe activity in reconstitution assays (Bechstedt & Brouhard 2012, Moores et al 2004). Rather, we only detected a minor misorientation of EB comets in our DCX-KO neurons (Fig. 3). The lack of change in EB comet behavior suggests that EB proteins outcompete DCX for their shared plus-end binding sites, e.g. via faster association kinetics (Reid et al 2019), differences in binding site preferences (Ettinger et al 2016), or exclusion of DCX from EB condensates (Song et al 2023).

DCX also shares its binding site with its close relative, DCLK1. Both proteins regulate neuronal migration and morphology (Friocourt et al 2007, Shin et al 2013), and double-KO mice have severe defects in brain development (Deuel et al 2006). Hence, DCLK1 might compensate for DCX-KO or interact differently with patient-mutant DCX. The kinase domain of DCLK1 is auto-regulatory (Agulto et al 2021), effectively tuning the affinity of DCLK1 for microtubules, which may impact DCX's affinity as well. Understanding the overlapping and independent roles of these two proteins is an important area of future research, including but not limited to their roles in the regulation of the tubulin code.

The PTMs of the tubulin code are frequently correlated; e.g., multiple PTMs are increased simultaneously by taxol (Hammond et al 2010), perhaps because stabilized microtubules have more time to accumulate PTMs. However, polyglutamylated microtubules specifically enhance detyrosination (Ebberink et al 2022), indicating a more specific correlation. In contrast, our work demonstrates that one PTM can be significantly reduced (polyglutamylation) while others remain constant, indicating that PTMs can be individually regulated.

Among the potential regulators of the tubulin code, our work has identified DCX as a key regulator of polyglumatylation, and more generally implicated MAPs in regulating tubulin PTMs. MAPs that regulate the tubulin code may share DCX's sensitivity to structural features of the microtubule lattice. If the tubulin code has "writers" (like TTLLs) and "readers" (like spastin and tau), then DCX could act as an "editor" that regulates the tubulin code to maintain the homeostasis of the neuronal microtubule cytoskeleton.

References

Agulto RL, Rogers MM, Tan TC, Ramkumar A, Downing AM, et al. 2021. Autoregulatory control of microtubule binding in doublecortin-like kinase 1. *Elife* 10

Akhmanova A, Steinmetz MO. 2015. Control of microtubule organization and dynamics: two ends in the limelight. *Nat Rev Mol Cell Biol* 16: 711-26

Alexander JE, Hunt DF, Lee MK, Shabanowitz J, Michel H, et al. 1991. Characterization of posttranslational modifications in neuron-specific class III beta-tubulin by mass spectrometry. *Proc Natl Acad Sci U S A* 88: 4685-9

Atherton J, Stouffer M, Francis F, Moores CA. 2022. Visualising the cytoskeletal machinery in neuronal growth cones using cryo-electron tomography. *J Cell Sci* 135

Audebert S, Desbruyeres E, Gruszczynski C, Koulakoff A, Gros F, et al. 1993. Reversible Polyglutamylation of Alpha-Tubulin and Beta-Tubulin and Microtubule Dynamics in Mouse-Brain Neurons. *Molecular Biology of the Cell* 4: 615-26

Baas PW, Black MM. 1990. Individual microtubules in the axon consist of domains that differ in both composition and stability. *J Cell Biol* 111: 495-509

Baas PW, Deitch JS, Black MM, Banker GA. 1988. Polarity orientation of microtubules in hippocampal neurons: uniformity in the axon and nonuniformity in the dendrite. *Proc Natl Acad Sci U S A* 85: 8335-9

Baek ST, Kerjan G, Bielas SL, Lee JE, Fenstermaker AG, et al. 2014. Off-target effect of doublecortin family shRNA on neuronal migration associated with endogenous microRNA dysregulation. *Neuron* 82: 1255-62

Bahi-Buisson N, Souville I, Fourniol FJ, Toussaint A, Moores CA, et al. 2013. New insights into genotype-phenotype correlations for the doublecortin-related lissencephaly spectrum. *Brain* 136: 223-44

Bai J, Ramos RL, Ackman JB, Thomas AM, Lee RV, LoTurco JJ. 2003. RNAi reveals doublecortin is required for radial migration in rat neocortex. *Nat Neurosci* 6: 1277-83

Balabanian L, Berger CL, Hendricks AG. 2017. Acetylated Microtubules Are Preferentially Bundled Leading to Enhanced Kinesin-1 Motility. *Biophys J* 113: 1551-60

Bechstedt S, Brouhard GJ. 2012. Doublecortin recognizes the 13-protofilament microtubule cooperatively and tracks microtubule ends. *Dev Cell* 23: 181-92

Bechstedt S, Lu K, Brouhard GJ. 2014. Doublecortin recognizes the longitudinal curvature of the microtubule end and lattice. *Curr Biol* 24: 2366-75

Belvindrah R, Natarajan K, Shabajee P, Bruel-Jungerman E, Bernard J, et al. 2017. Mutation of the alpha-tubulin Tuba1a leads to straighter microtubules and perturbs neuronal migration. *J Cell Biol* 216: 2443-61

Bentley M, Decker H, Luisi J, Banker G. 2015. A novel assay reveals preferential binding between Rabs, kinesins, and specific endosomal subpopulations. *J Cell Biol* 208: 273-81

Bielas SL, Serneo FF, Chechlacz M, Deerinck TJ, Perkins GA, et al. 2007. Spinophilin facilitates dephosphorylation of doublecortin by PP1 to mediate microtubule bundling at the axonal wrist. *Cell* 129: 579-91

Bilimoria PM, de la Torre-Ubieta L, Ikeuchi Y, Becker EB, Reiner O, Bonni A. 2010. A JIP3-regulated GSK3beta/DCX signaling pathway restricts axon branching. *J Neurosci* 30: 16766-76

Bodakuntla S, Jijumon AS, Villablanca C, Gonzalez-Billault C, Janke C. 2019. Microtubule-Associated Proteins: Structuring the Cytoskeleton. *Trends Cell Biol* 29: 804-19

Bodakuntla S, Yuan X, Genova M, Gadadhar S, Leboucher S, et al. 2021. Distinct roles of alpha- and beta-tubulin polyglutamylation in controlling axonal transport and in neurodegeneration. *EMBO J* 40: e108498

Bonnet C, Boucher D, Lazereg S, Pedrotti B, Islam K, et al. 2001. Differential binding regulation of microtubule-associated proteins MAP1A, MAP1B, and MAP2 by tubulin polyglutamylation. *J Biol Chem* 276: 12839-48

Boucher D, Larcher JC, Gros F, Denoulet P. 1994. Polyglutamylation of tubulin as a progressive regulator of in vitro interactions between the microtubule-associated protein Tau and tubulin. *Biochemistry* 33: 12471-7

Buchsbaum IY, Cappello S. 2019. Neuronal migration in the CNS during development and disease: insights from in vivo and in vitro models. *Development* 146

Burger D, Stihle M, Sharma A, Di Lello P, Benz J, et al. 2016. Crystal Structures of the Human Doublecortin C- and N-terminal Domains in Complex with Specific Antibodies. *J Biol Chem* 291: 16292-306

Chai X, Fan L, Shao H, Lu X, Zhang W, et al. 2015. Reelin Induces Branching of Neurons and Radial Glial Cells during Corticogenesis. *Cereb Cortex* 25: 3640-53

Chaudhary AR, Berger F, Berger CL, Hendricks AG. 2018. Tau directs intracellular trafficking by regulating the forces exerted by kinesin and dynein teams. *Traffic* 19: 111-21

Chazeau A, Katrukha EA, Hoogenraad CC, Kapitein LC. 2016. Studying neuronal microtubule organization and microtubule-associated proteins using single molecule localization microscopy. *Methods Cell Biol* 131: 127-49

Cohen D, Segal M, Reiner O. 2008. Doublecortin supports the development of dendritic arbors in primary hippocampal neurons. *Dev Neurosci* 30: 187-99

Coles CH, Bradke F. 2015. Coordinating neuronal actin-microtubule dynamics. *Curr Biol* 25: R677-91

Cooper JA. 2013. Cell biology in neuroscience: mechanisms of cell migration in the nervous system. *J Cell Biol* 202: 725-34

Corbo JC, Deuel TA, Long JM, LaPorte P, Tsai E, et al. 2002. Doublecortin is required in mice for lamination of the hippocampus but not the neocortex. *J Neurosci* 22: 7548-57

Cueva JG, Hsin J, Huang KC, Goodman MB. 2012. Posttranslational acetylation of alpha-tubulin constrains protofilament number in native microtubules. *Curr Biol* 22: 1066-74

Dehmelt L, Halpain S. 2004. Actin and microtubules in neurite initiation: are MAPs the missing link? *J Neurobiol* 58: 18-33

Dema A, Charafeddine R, Rahgozar S, van Haren J, Wittmann T. 2023. Growth cone advance requires EB1 as revealed by genomic replacement with a light-sensitive variant. *Elife* 12

des Portes V, Francis F, Pinard JM, Desguerre I, Moutard ML, et al. 1998. doublecortin is the major gene causing X-linked subcortical laminar heterotopia (SCLH). *Hum Mol Genet* 7: 1063-70

Deuel TA, Liu JS, Corbo JC, Yoo SY, Rorke-Adams LB, Walsh CA. 2006. Genetic interactions between doublecortin and doublecortin-like kinase in neuronal migration and axon outgrowth. *Neuron* 49: 41-53

Dogterom M, Kerssemakers JW, Romet-Lemonne G, Janson ME. 2005. Force generation by dynamic microtubules. *Curr Opin Cell Biol* 17: 67-74

Dogterom M, Koenderink GH. 2019. Actin-microtubule crosstalk in cell biology. *Nat Rev Mol Cell Biol* 20: 38-54

Ebberink E, Fernandes S, Hatzopoulos G, Agashe N, Guidotti N, et al. 2022. Tubulin engineering by semisynthesis reveals that polyglutamylation directs detyrosination. *bioRxiv*: 2022.09.20.508649

Edde B, Rossier J, Le Caer JP, Desbruyeres E, Gros F, Denoulet P. 1990. Posttranslational glutamylation of alpha-tubulin. *Science* 247: 83-5

Ershov D, Phan MS, Pylvanainen JW, Rigaud SU, Le Blanc L, et al. 2022. TrackMate 7: integrating state-of-the-art segmentation algorithms into tracking pipelines. *Nat Methods* 19: 829-32

Ettinger A, van Haren J, Ribeiro SA, Wittmann T. 2016. Doublecortin Is Excluded from Growing Microtubule Ends and Recognizes the GDP-Microtubule Lattice. *Curr Biol* 26: 1549-55

Feng Y, Walsh CA. 2001. Protein-protein interactions, cytoskeletal regulation and neuronal migration. *Nat Rev Neurosci* 2: 408-16

Fourniol FJ, Sindelar CV, Amigues B, Clare DK, Thomas G, et al. 2010. Template-free 13-protofilament microtubule-MAP assembly visualized at 8 A resolution. *J Cell Biol* 191: 463-70

Francis F, Koulakoff A, Boucher D, Chafey P, Schaar B, et al. 1999. Doublecortin is a developmentally regulated, microtubule-associated protein expressed in migrating and differentiating neurons. *Neuron* 23: 247-56

Friocourt G, Koulakoff A, Chafey P, Boucher D, Fauchereau F, et al. 2003. Doublecortin functions at the extremities of growing neuronal processes. *Cereb Cortex* 13: 620-6

Friocourt G, Liu JS, Antypa M, Rakic S, Walsh CA, Parnavelas JG. 2007. Both doublecortin and doublecortin-like kinase play a role in cortical interneuron migration. *J Neurosci* 27: 3875-83

Fu X, Brown KJ, Yap CC, Winckler B, Jaiswal JK, Liu JS. 2013. Doublecortin (Dcx) family proteins regulate filamentous actin structure in developing neurons. *J Neurosci* 33: 709-21

Fu X, Rao L, Li P, Liu X, Wang Q, et al. 2022. Doublecortin and JIP3 are neural-specific counteracting regulators of dynein-mediated retrograde trafficking. *Elife* 11

Gallo G, Letourneau PC. 1999. Different contributions of microtubule dynamics and transport to the growth of axons and collateral sprouts. *J Neurosci* 19: 3860-73

Garnham CP, Vemu A, Wilson-Kubalek EM, Yu I, Szyk A, et al. 2015. Multivalent Microtubule Recognition by Tubulin Tyrosine Ligase-like Family Glutamylases. *Cell* 161: 1112-23

Genova M, Grycova L, Puttrich V, Magiera MM, Lansky Z, et al. 2023. Tubulin polyglutamylation differentially regulates microtubule-interacting proteins. *EMBO J* 42: e112101

Gleeson JG, Allen KM, Fox JW, Lamperti ED, Berkovic S, et al. 1998. Doublecortin, a brain-specific gene mutated in human X-linked lissencephaly and double cortex syndrome, encodes a putative signaling protein. *Cell* 92: 63-72

Gleeson JG, Lin PT, Flanagan LA, Walsh CA. 1999. Doublecortin is a microtubule-associated protein and is expressed widely by migrating neurons. *Neuron* 23: 257-71

Guardia CM, Farias GG, Jia R, Pu J, Bonifacino JS. 2016. BORC Functions Upstream of Kinesins 1 and 3 to Coordinate Regional Movement of Lysosomes along Different Microtubule Tracks. *Cell Rep* 17: 1950-61

Gumy LF, Katrukha EA, Grigoriev I, Jaarsma D, Kapitein LC, et al. 2017. MAP2 Defines a Pre-axonal Filtering Zone to Regulate KIF1- versus KIF5-Dependent Cargo Transport in Sensory Neurons. *Neuron* 94: 347-62 e7

Gupta A, Sanada K, Miyamoto DT, Rovelstad S, Nadarajah B, et al. 2003. Layering defect in p35 deficiency is linked to improper neuronal-glial interaction in radial migration. *Nat Neurosci* 6: 1284-91

Hammond JW, Huang CF, Kaech S, Jacobson C, Banker G, Verhey KJ. 2010. Posttranslational modifications of tubulin and the polarized transport of kinesin-1 in neurons. *Mol Biol Cell* 21: 572-83

Herculano-Houzel S. 2009. The human brain in numbers: a linearly scaled-up primate brain. *Front Hum Neurosci* 3: 31

Hirokawa N, Noda Y, Tanaka Y, Niwa S. 2009. Kinesin superfamily motor proteins and intracellular transport. *Nat Rev Mol Cell Biol* 10: 682-96

Hoff KJ, Aiken JE, Gutierrez MA, Franco SJ, Moore JK. 2022. TUBA1A tubulinopathy mutants disrupt neuron morphogenesis and override XMAP215/Stu2 regulation of microtubule dynamics. *Elife* 11

Homma N, Takei Y, Tanaka Y, Nakata T, Terada S, et al. 2003. Kinesin superfamily protein 2A (KIF2A) functions in suppression of collateral branch extension. *Cell* 114: 229-39

Howard J, Hyman AA. 2007. Microtubule polymerases and depolymerases. *Curr Opin Cell Biol* 19: 31-5

Iwanski MK, Kapitein LC. 2023. Cellular cartography: Towards an atlas of the neuronal microtubule cytoskeleton. *Front Cell Dev Biol* 11: 1052245

Janke C, Magiera MM. 2020. The tubulin code and its role in controlling microtubule properties and functions. *Nat Rev Mol Cell Biol* 21: 307-26

Janke C, Rogowski K, Wloga D, Regnard C, Kajava AV, et al. 2005. Tubulin polyglutamylase enzymes are members of the TTL domain protein family. *Science* 308: 1758-62

Jean DC, Baas PW, Black MM. 2012. A novel role for doublecortin and doublecortin-like kinase in regulating growth cone microtubules. *Hum Mol Genet* 21: 5511-27

Kalil K, Dent EW. 2014. Branch management: mechanisms of axon branching in the developing vertebrate CNS. *Nat Rev Neurosci* 15: 7-18

Kapitein LC, Hoogenraad CC. 2015. Building the Neuronal Microtubule Cytoskeleton. *Neuron* 87: 492-506

Kappeler C, Saillour Y, Baudoin JP, Tuy FP, Alvarez C, et al. 2006. Branching and nucleokinesis defects in migrating interneurons derived from doublecortin knockout mice. *Hum Mol Genet* 15: 1387-400

Kawauchi T, Hoshino M. 2008. Molecular pathways regulating cytoskeletal organization and morphological changes in migrating neurons. *Dev Neurosci* 30: 36-46

Kim MH, Cierpicki T, Derewenda U, Krowarsch D, Feng Y, et al. 2003. The DCX-domain tandems of doublecortin and doublecortin-like kinase. *Nat Struct Biol* 10: 324-33

Koizumi H, Higginbotham H, Poon T, Tanaka T, Brinkman BC, Gleeson JG. 2006. Doublecortin maintains bipolar shape and nuclear translocation during migration in the adult forebrain. *Nat Neurosci* 9: 779-86

Lacroix B, van Dijk J, Gold ND, Guizetti J, Aldrian-Herrada G, et al. 2010. Tubulin polyglutamylation stimulates spastin-mediated microtubule severing. *J Cell Biol* 189: 945-54

Leger PL, Souville I, Boddaert N, Elie C, Pinard JM, et al. 2008. The location of DCX mutations predicts malformation severity in X-linked lissencephaly. *Neurogenetics* 9: 277-85

Lessard DV, Zinder OJ, Hotta T, Verhey KJ, Ohi R, Berger CL. 2019. Polyglutamylation of tubulin's C-terminal tail controls pausing and motility of kinesin-3 family member KIF1A. *J Biol Chem* 294: 6353-63

Li H, Mao S, Wang H, Zen K, Zhang C, Li L. 2014. MicroRNA-29a modulates axon branching by targeting doublecortin in primary neurons. *Protein Cell* 5: 160-9

Lindhout FW, Kooistra R, Portegies S, Herstel LJ, Stucchi R, et al. 2020. Quantitative mapping of transcriptome and proteome dynamics during polarization of human iPSC-derived neurons. *Elife* 9

Lipka J, Kapitein LC, Jaworski J, Hoogenraad CC. 2016. Microtubule-binding protein doublecortin-like kinase 1 (DCLK1) guides kinesin-3-mediated cargo transport to dendrites. *EMBO J* 35: 302-18

Liu JS, Schubert CR, Fu X, Fourniol FJ, Jaiswal JK, et al. 2012. Molecular basis for specific regulation of neuronal kinesin-3 motors by doublecortin family proteins. *Mol Cell* 47: 707-21

Maday S, Twelvetrees AE, Moughamian AJ, Holzbaur EL. 2014. Axonal transport: cargo-specific mechanisms of motility and regulation. *Neuron* 84: 292-309

Magiera MM, Singh P, Gadadhar S, Janke C. 2018. Tubulin Posttranslational Modifications and Emerging Links to Human Disease. *Cell* 173: 1323-27

Mahalingan KK, Keith Keenan E, Strickland M, Li Y, Liu Y, et al. 2020. Structural basis for polyglutamate chain initiation and elongation by TTLL family enzymes. *Nat Struct Mol Biol* 27: 802-13

Manka SW, Moores CA. 2018. The role of tubulin-tubulin lattice contacts in the mechanism of microtubule dynamic instability. *Nat Struct Mol Biol* 25: 607-15

Manka SW, Moores CA. 2020. Pseudo-repeats in doublecortin make distinct mechanistic contributions to microtubule regulation. *EMBO Rep* 21: e51534

Martini FJ, Valiente M, Lopez Bendito G, Szabo G, Moya F, et al. 2009. Biased selection of leading process branches mediates chemotaxis during tangential neuronal migration. *Development* 136: 41-50

Maurer SP, Fourniol FJ, Bohner G, Moores CA, Surrey T. 2012. EBs recognize a nucleotide-dependent structural cap at growing microtubule ends. *Cell* 149: 371-82

McKenney RJ, Huynh W, Vale RD, Sirajuddin M. 2016. Tyrosination of alpha-tubulin controls the initiation of processive dynein-dynactin motility. *EMBO J* 35: 1175-85

Menon S, Gupton SL. 2016. Building Blocks of Functioning Brain: Cytoskeletal Dynamics in Neuronal Development. *Int Rev Cell Mol Biol* 322: 183-245

Monroy BY, Sawyer DL, Ackermann BE, Borden MM, Tan TC, Ori-McKenney KM. 2018. Competition between microtubule-associated proteins directs motor transport. *Nat Commun* 9: 1487

Monroy BY, Tan TC, Oclaman JM, Han JS, Simo S, et al. 2020. A Combinatorial MAP Code Dictates Polarized Microtubule Transport. *Dev Cell* 53: 60-72 e4

Moores CA, Perderiset M, Francis F, Chelly J, Houdusse A, Milligan RA. 2004. Mechanism of microtubule stabilization by doublecortin. *Mol Cell* 14: 833-9

Moores CA, Perderiset M, Kappeler C, Kain S, Drummond D, et al. 2006. Distinct roles of doublecortin modulating the microtubule cytoskeleton. *EMBO J* 25: 4448-57

Moutin MJ, Bosc C, Peris L, Andrieux A. 2021. Tubulin post-translational modifications control neuronal development and functions. *Dev Neurobiol* 81: 253-72

Nadarajah B, Parnavelas JG. 2002. Modes of neuronal migration in the developing cerebral cortex. *Nat Rev Neurosci* 3: 423-32

Omori Y, Suzuki M, Ozaki K, Harada Y, Nakamura Y, et al. 1998. Expression and chromosomal localization of KIAA0369, a putative kinase structurally related to Doublecortin. *J Hum Genet* 43: 169-77

Pacheco A, Gallo G. 2016. Actin filament-microtubule interactions in axon initiation and branching. *Brain Res Bull* 126: 300-10

Portran D, Schaedel L, Xu Z, Thery M, Nachury MV. 2017. Tubulin acetylation protects long-lived microtubules against mechanical ageing. *Nat Cell Biol* 19: 391-98

Prowse ENP, Chaudhary AR, Sharon D, Hendricks AG. 2023. Huntingtin S421 phosphorylation increases kinesin and dynein engagement on early endosomes and lysosomes. *Biophys J* 122: 1168-84

Pu J, Guardia CM, Keren-Kaplan T, Bonifacino JS. 2016. Mechanisms and functions of lysosome positioning. *J Cell Sci* 129: 4329-39

Rafiei A, Cruz Tetlalmatzi S, Edrington CH, Lee L, Crowder DA, et al. 2022. Doublecortin engages the microtubule lattice through a cooperative binding mode involving its C-terminal domain. *Elife* 11

Rakic P. 1972. Mode of cell migration to the superficial layers of fetal monkey neocortex. *J Comp Neurol* 145: 61-83

Ramkumar A, Jong BY, Ori-McKenney KM. 2018. ReMAPping the microtubule landscape: How phosphorylation dictates the activities of microtubule-associated proteins. *Dev Dyn* 247: 138-55

Redeker V, Melki R, Prome D, Le Caer JP, Rossier J. 1992. Structure of tubulin C-terminal domain obtained by subtilisin treatment. The major alpha and beta tubulin isotypes from pig brain are glutamylated. *FEBS Lett* 313: 185-92

Reid TA, Coombes C, Mukherjee S, Goldblum RR, White K, et al. 2019. Structural state recognition facilitates tip tracking of EB1 at growing microtubule ends. *Elife* 8

Rogowski K, van Dijk J, Magiera MM, Bosc C, Deloulme JC, et al. 2010. A family of protein-deglutamylating enzymes associated with neurodegeneration. *Cell* 143: 564-78

Roll-Mecak A. 2020. The Tubulin Code in Microtubule Dynamics and Information Encoding. *Dev Cell* 54: 7-20

Roll-Mecak A, Vale RD. 2006. Making more microtubules by severing: a common theme of noncentrosomal microtubule arrays? *J Cell Biol* 175: 849-51

Sapir T, Horesh D, Caspi M, Atlas R, Burgess HA, et al. 2000. Doublecortin mutations cluster in evolutionarily conserved functional domains. *Hum Mol Genet* 9: 703-12

Schaedel L, John K, Gaillard J, Nachury MV, Blanchoin L, Thery M. 2015. Microtubules self-repair in response to mechanical stress. *Nat Mater* 14: 1156-63

Shashi V, Magiera MM, Klein D, Zaki M, Schoch K, et al. 2018. Loss of tubulin deglutamylase CCP1 causes infantile-onset neurodegeneration. *EMBO J* 37

Shin E, Kashiwagi Y, Kuriu T, Iwasaki H, Tanaka T, et al. 2013. Doublecortin-like kinase enhances dendritic remodelling and negatively regulates synapse maturation. *Nat Commun* 4: 1440

Siahaan V, Tan R, Humhalova T, Libusova L, Lacey SE, et al. 2022. Microtubule lattice spacing governs cohesive envelope formation of tau family proteins. *Nat Chem Biol* 18: 1224-35

Sirajuddin M, Rice LM, Vale RD. 2014. Regulation of microtubule motors by tubulin isotypes and post-translational modifications. *Nat Cell Biol* 16: 335-44

Song X, Yang F, Yang T, Wang Y, Ding M, et al. 2023. Phase separation of EB1 guides microtubule plus-end dynamics. *Nat Cell Biol* 25: 79-91

Tan R, Lam AJ, Tan T, Han J, Nowakowski DW, et al. 2019. Microtubules gate tau condensation to spatially regulate microtubule functions. *Nat Cell Biol* 21: 1078-85

Tanaka T, Koizumi H, Gleeson JG. 2006. The doublecortin and doublecortin-like kinase 1 genes cooperate in murine hippocampal development. *Cereb Cortex* 16 Suppl 1: i69-73

Tas RP, Chazeau A, Cloin BMC, Lambers MLA, Hoogenraad CC, Kapitein LC. 2017. Differentiation between Oppositely Oriented Microtubules Controls Polarized Neuronal Transport. *Neuron* 96: 1264-71 e5

Taylor KR, Holzer AK, Bazan JF, Walsh CA, Gleeson JG. 2000. Patient mutations in doublecortin define a repeated tubulin-binding domain. *J Biol Chem* 275: 34442-50

Tinevez JY, Perry N, Schindelin J, Hoopes GM, Reynolds GD, et al. 2017. TrackMate: An open and extensible platform for single-particle tracking. *Methods* 115: 80-90

Tint I, Jean D, Baas PW, Black MM. 2009. Doublecortin associates with microtubules preferentially in regions of the axon displaying actin-rich protrusive structures. *J Neurosci* 29: 10995-1010

Tsai LH, Gleeson JG. 2005. Nucleokinesis in neuronal migration. *Neuron* 46: 383-8

Umeshima H, Hirano T, Kengaku M. 2007. Microtubule-based nuclear movement occurs independently of centrosome positioning in migrating neurons. *Proc Natl Acad Sci U S A* 104: 16182-7

Valenstein ML, Roll-Mecak A. 2016. Graded Control of Microtubule Severing by Tubulin Glutamylation. *Cell* 164: 911-21

van Dijk J, Rogowski K, Miro J, Lacroix B, Edde B, Janke C. 2007. A targeted multienzyme mechanism for selective microtubule polyglutamylation. *Mol Cell* 26: 437-48

Vemu A, Szczesna E, Zehr EA, Spector JO, Grigorieff N, et al. 2018. Severing enzymes amplify microtubule arrays through lattice GTP-tubulin incorporation. *Science* 361

Verhey KJ, Gaertig J. 2007. The tubulin code. *Cell Cycle* 6: 2152-60

Verhey KJ, Ohi R. 2023. Causes, costs and consequences of kinesin motors communicating through the microtubule lattice. *J Cell Sci* 136

Wolff A, de Nechaud B, Chillet D, Mazarguil H, Desbruyeres E, et al. 1992. Distribution of glutamylated alpha and beta-tubulin in mouse tissues using a specific monoclonal antibody, GT335. *Eur J Cell Biol* 59: 425-32

Yang CH, Horwitz SB. 2017. Taxol((R)): The First Microtubule Stabilizing Agent. *Int J Mol Sci* 18

Yap CC, Digilio L, McMahon L, Roszkowska M, Bott CJ, et al. 2016. Different Doublecortin (DCX) Patient Alleles Show Distinct Phenotypes in Cultured Neurons: EVIDENCE FOR DIVERGENT LOSS-OF-FUNCTION AND "OFF-PATHWAY" CELLULAR MECHANISMS. *J Biol Chem* 291: 26613-26

Yu W, Qiang L, Solowska JM, Karabay A, Korulu S, Baas PW. 2008. The microtubule-severing proteins spastin and katanin participate differently in the formation of axonal branches. *Mol Biol Cell* 19: 1485-98

Acknowledgements

We would like to thank current members of the Brouhard, Hendricks and Bechstedt labs, for fruitful discussions during all phases of this project, and more particularly past members Hadrien Mary and Piper Stevens for their help in code writing. Many thanks to Geneviève Dorval and Thomas Durcan for thoughtful support with the use of iPSCs and CRISPR methods. We would also like to acknowledge the McGill University Advanced BioImaging Facility (ABIF), RRID: SCR_017697, the Flow cytometry core facility of the Life Science Complex, the Genome Québec sequencing platform, and their personal for providing services and helpful advice for data collection and analysis.

Author contributions

Conceptualization and experimental design: GJB, MS, and AGH. Experimental procedures: MS, Data analysis: MS and EP, Manuscript writing: MS, GJB, and AGH. All authors participated in manuscript edition. Funding acquisition: GJB and AGH.

Competing interest statement

The authors declare no competing interests.

Materials and Methods

iPSCs origin, maintenance, and differentiation

hiPSCs initial stocks were obtained from the C-BIGR repository at the Montreal Neurological Institute. The AIW2-2 line comes from an unaffected male donor and was generated from PBMCs. The cells were grown on Matrigel coated surfaces in mTeSR plus media in feeder-free conditions, they were passaged using Gentle Cell dissociation reagent (GCDR) and supplemented with 10uM Y-27362 for 24h when required after thawing, gene-editing or low-density plating. hiPSCs were induced into Neuronal progenitor cells using Stemdiff Smadi induction media provided by Stemcell technologies. Briefly, the hiPSCs were seeded in a monolayer at high density and feeded with fresh induction media every other day for 6-12 days. Then the cells were dissociated using accutase and amplified on PO-laminin coated plates for an additional period of 10-15 days before cryopreservation. Terminal differentiation into cortical neurons was performed using commercially available BrainPhys and supplemented as required by manufacturer's guidelines. NPCs were seeded on PO-Laminin coated dishes or coverslips at variable densities depending on the experiment and were differentiated for DIV3 days. Cell fixations was performed following (Chazeau et al 2016) method: after 1,5min incubation in extraction buffer when specified (PIPES 80mM, EGTA 1mM, MgCl2 7mM, NaCl 150mM, D-Glucose 5mM, Triton X-100 0.3%, Glutaraldehyde 0.25%), PFA 4% was applied to the cells maintained at 37°C for 15min before rinsing and storage in PBS until further use.

CRISPR gene-edition

AIW2-2 hiPSCs line was gene edited using CRISPR/Cas9 techniques. gRNAs for DCX Knock-In were designed using the CRISPRdirect online tool. They were cloned into the pX458 plasmid generously gifted by Feng Zhang (#48138), using the BBsI restriction site. The newly generated plasmids were transformed into Stbl3 strains and amplified according to nucleobond Maxiprep kit supplier's recommendations. The actual gene edition was performed using electroporation, as follows: the hiPSCs were detached from the substrate using accutase, counted and about 5millions cells were resuspended in 100ul of cold Internal Neuronal Buffer (KCl 135mM, CaCl2 200µM, MgCl2 2mM, HEPES 10mM, EGTA 5mM). The cell suspension was added to 5ug of gRNA/Cas9 plasmid with 30ug of the corresponding single stranded template before application to a 100ul BTX cuvette. The BTX Gemini X2 twinwave electroporator was used to deliver a single 10ms pulse at 60V. Warmed up mTeSR was then added on top of the electroporated cells before transfer of the cell suspension to a new matrigel coated dish with rock inhibitor supplemented mTeSR. Three days post-electroporation, the cells were again dissociated from the substrate using accutase and were passed through a 70um strainer before FACs-sorting for GFP positive cells. The cell sorting was performed in the Flow Cytometry Core Facility for flow cytometry and single cell analysis of the Life Science Complex and supported by funding from the Canadian Foundation for Innovation. The positive cells were seeded in individual wells of 96 well plates and left to grow for about 2 weeks. For proper recovery and growth of the cells, rock inhibitor or CloneR were kept in the mTeSR media for 24 to 72h post-sorting. After sufficient growth of individual hiPSCs clones in the 96 well plates, the clones were collected and split in two in order to amplify the cells and screen for indels in extracted genomic DNA. For screening, each clone's genomic DNA was extracted in Quick extract buffer, amplified by PCR and depending on the profile of the PCR product and response to T7 assay, the clones were subjected to Sanger sequencing performed at Genome Québec.

Cell preparation

Following fixation, the coverslips were quenched in NaBH4 at 1mg/ml for 10min, then they were subjected to permeabilization in PBS-Triton 0.5% for 10min. Unspecific bindings were blocked by bathing the coverslips in PBS-Triton0.1%-BSA3% for 30 min before incubation with the primary antibodies overnight at 4°C. Incubation with the secondary antibodies were done at room temperature for 1h, before a DAPI stain and mounting of the coverslips with Fluorsave.

Transient expression of EB3-mCherry or DCX-GFP were performed using electroporation. Briefly, the NPCs were dissociated and about 0.5-1 million

cells were mixed with 5ug of plasmid in 200ul of INB. The electroporation was performed with a 1ms pulse at 350V in 620 BTX cuvettes. The cells were then seeded on glass bottom dishes or coverslips and imaged in BrainPhys or fixed as previously described. When dyes were used to look at specific structures in live neurons, they were all diluted in warmed up BrainPhys and incubated for specified timing with the cells before removal and imaging. SiR tubulin 100nM 30min, CellMask Green Actin 0.5X 30min, Lysotracker 50nM 10min, Syto Nucleus Deep red 250nM 30min.

Imaging and analysis

Image collection for this manuscript was performed in the McGill University Advanced BioImaging Facility (ABIF), RRID:SCR_017697. All images were analyzed primarily in Fiji and processed using Microsoft office excel, and python. The Zeiss LSM710 inverted confocal and X-Cite 120 LED with Zen 2.0 software were used to screen and acquire images of fixed samples. The objectives 10X EC plan neofluar NA 0.3, and 63X plan apochromat NA 1.4 oil were used. Intensity profiles in fixed samples were obtained from thick ROI lines drawn on neurites from the tip to the cell body, or by creation of a dilated mask of the DAPI signal for cell bodies. The intensity per pixel was interpolated from pixels along the width of the line, the generated profiles were then further compiled with other images using excel and python. For intensity quantification in entire field of views, all images were acquired in the same laser power and gain conditions, the tubulin B3 or tyrosinated (YL1/2) microtubule signal was used as a mask for cells and intensity with the other channels were measured inside the mask and normalized to the mask intensity. The number of branches per cell were manually counted and their length measured with fiji line tools.

The Quorum WaveFX-X1 spinning disk confocal system on a Leica DMI6000B inverted microscope equipped with a Photometrics prime BSI Cmos camera was used for short term live-cell imaging. We used the 63X plan apochromat NA 1.4 oil objective and the Metamorph software to record EB3mCherry and lysotracker dynamics. All timelapse movies recorded were 2min total, and live cells were never imaged for more than 1h. For EB3, images were taken with 2s interval, in neurons with low-medium expression levels. Kymographs were done from wide multipoint ROI lines drawn on processes from the tip to the cell body. Then straight ROI lines were drawn on each comet and a homemade python script extracted the comet direction, lifetime, length and growth rate. For each cell, the growth cone and process areas were measured by thresholding a maximum projection of the timelapse. All further analyses were made in python and used a mean value per cell.

For lysotracker data acquisition, the timelapses were 500ms interval. Straight sections of the processes excluding cell bodies were selected using the polygon ROI tool and cargo trajectories were analysed inside, using the Trackmate plugin (Ershov et al 2022, Tinevez et al 2017). Trackmate was set up to use the LoG detector to identify 1µm diameter spots, with sub-pixel localization. Then the simple LAP tracker was used to define and filter trajectories that were exported as xml files. To analyze the TrackMate data, we had previously written custom MATLAB codes (Prowse et al 2023), available on Github: https://github.com/hendricks-lab. For each trajectory, we converted coordinate x and y position values to a single position vector with respect to the location of the soma. This position vector had a positive value when the tracked cargo moved anterogradely, and a negative value when moving retrogradely, as shown in Figure 4. Using the position vector, we reduced the noise using a Savitzky-Golay smoothing filter of power 2 and span of 9 and segmented the trajectory into runs at each inflection point. These runs were used in the run length and velocity analysis. Between each inflection point, we determined the absolute value of the cargo's displacement. If the displacement within the run was larger than 2 µm, the run was considered processive, while if it was between 0.03 µm and 2 µm, the run was categorized as diffusive, and finally if the displacement was 0.03 µm or smaller, the run was considered stationary. The threshold for a run to be considered processive was determined by plotting the α value of processive runs compared to that of diffusive runs, as well as the directional bias of diffusive and processive runs. We determined that 2 µm was optimal because the processive runs had an α value near 2, while the diffusive runs had an α near 1, as expected. We also observed that there was no directional bias for diffusive runs at the set minimum run length threshold, indicating the runs are purely diffusive. We then determined the run length and velocity per trajectory by taking the mean of the processive runs or processive runs over time, respectively, for each trajectory. We calculated the α by calculating the slope of the mean squared displacement plot for each trajectory and subsequently taking the mean for each cell. We calculated mean squared displacement using a time average for time intervals from the exposure time of 0.5 s up to 20 s. We used (Eq. 1) to calculate the mean squared displacement (MSD), where t is the frame, τ is the time interval, and x is the position vector value at the specified time.

$$MSD = {}^{1}/_{\tau - t} \sum_{t=0}^{\tau - t} (x_{t+\tau} - x_t)^2 \ \ (Eq. 1)$$

The first 5 s of log-log plot of the mean squared displacement is used to calculate the α value for each trajectory, to ensure only the linear portion is fitted. We calculated the radius of gyration (Rg) using (Eq. 2). Here, r represents the sum of the squared x and y components, and N represents the number of position values in the entire trajectory.

$$R_g^2 = {}^{1}/_{N} \sum_{k=1}^{N} (\boldsymbol{r_k} - \boldsymbol{r_{mean}})^2 \ (Eq. 2)$$

To determine the directional bias, we determined the fraction of time the processive runs spent moving anterogradely compared to retrogradely, using the identified processive runs from the previously described function analyzing run length and velocity. To calculate the fraction of processive, stationary, and diffusive runs, we calculated the fraction of time for each run within each trajectory spent in each of these states, as defined by the previously described thresholds.

The perkin-elmer high content screening microscope operaphenix in confocal mode with the 20X NA 1.0 water objective and the Harmony 9.0 software were used for long time recording of neuronal movements and branch dynamics. Images were taken at 5-10min interval for 8 to 15h. For each imaging session, multiple FOV from the same well were taken and analysed individually. Nuclei tracking was done using trackmate within an automated python-based pipeline. The LoG detector and LAP simple tracker were also used with subpixel detection of 10µm spots, and 40µm maximum linking distance. Trajectories and spot data were exported as xml files, visually checked, and compiled within python.

Statistical analysis

All statistical tests used are indicated in the figure legends: Kruskal-Wallis non parametric H test, Mann-Whitney non parametric U test, or Student's t test. Pvalues were considered nonsignificant when above 0.05.

For the lysotracker dataset: For each per trajectory analysis, we took 1000 bootstrapped means with replacement and averaged them the same number of times as the minimum number of trajectories from either dataset. We then compared these means by subtracting the DCX-KO data from the control data and comparing the fraction of the difference distribution overlapping with 0. If this fraction was less than 0.05%, then we considered it a statistically significant difference, with a p value equal to the fraction that overlaps with the 0 line. Each value calculated per cell was analyzed using Student's two-tailed t test.

Western blots

The cells were lysed by incubation in cold RIPA or 2X SDS loading buffer (125mM Tris-HCl pH 6.8, 20% glycerol, 0.04% Bromophenol blue, 4% SDS, 100mM DTT) and were collected by scraping the plates. Lysates in RIPA buffer were supplemented with complete-T for long term storage. Before loading onto a 12% acrylamide gel, the lysates in RIPA were mixed with 2X SDS loading buffer and all samples were sonicated, spun down and boiled for 10min at 95°C. Electrophoresis was done in MOPS buffer at 160 constant voltage, then proteins were transferred to nitrocellulose membranes and blocked in 5% Milk. Primary antibodies were diluted according to the key resources sheet and incubated with the membrane at 4°C overnight. The membranes were rinsed with TBST and incubated for 2h with anti-HRP secondary antibodies. The proteins were revealed using ECL pico, and 2s-30min membrane exposure to Diamed films.

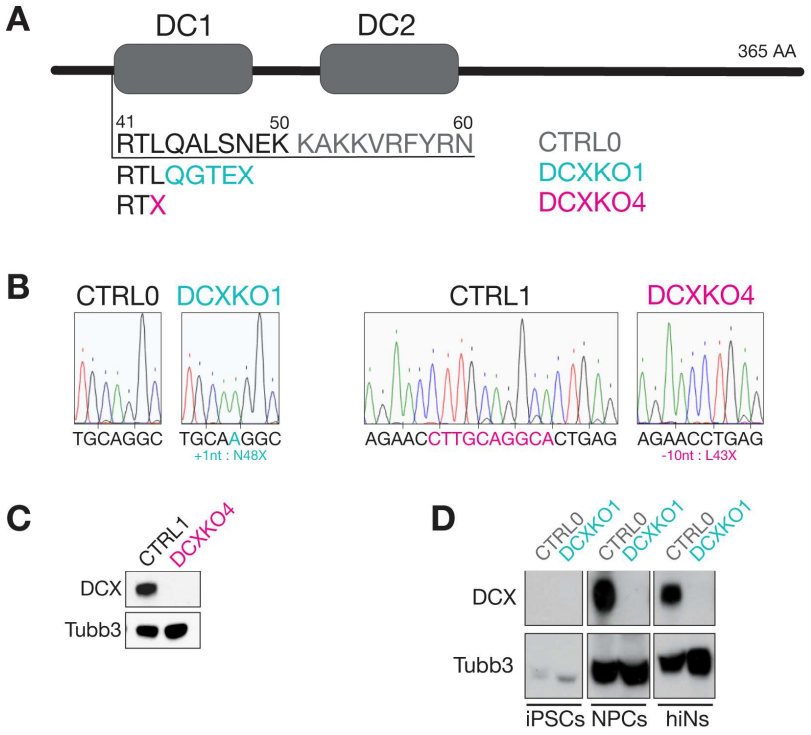

Figure S1: Engineering and sequences DCXKO1 and DCXKO4. (A) DCX contains two microtubule binding domains, DC1 and DC2. DCX-KO cells were obtained by indels introduced in Dcx's gene sequence before DC1. CTRL0/CTRL1, DCXKO1 and DCXKO4 amino acid sequences are shown from residue 41 to 60. The asterisk shows the indel location and the resulting amino acid sequence. **(B)** Chromatograms showing nucleotide sequences for CTRL0, DCXKO1, CTRL1 and DCXKO4, with indels highlighted below. **(C)** Immunoblot of CTRL1 and DCXKO4 neuron lysates at DIV3, with antibodies against Tubulin-β3 and DCX. **(D)** Immunoblot of CTRL0 and DCXKO1 lysates at the iPSCs stage, the NPCs stage and the neuronal stage at DIV3, with antibodies against Tubulin-β3 and DCX.

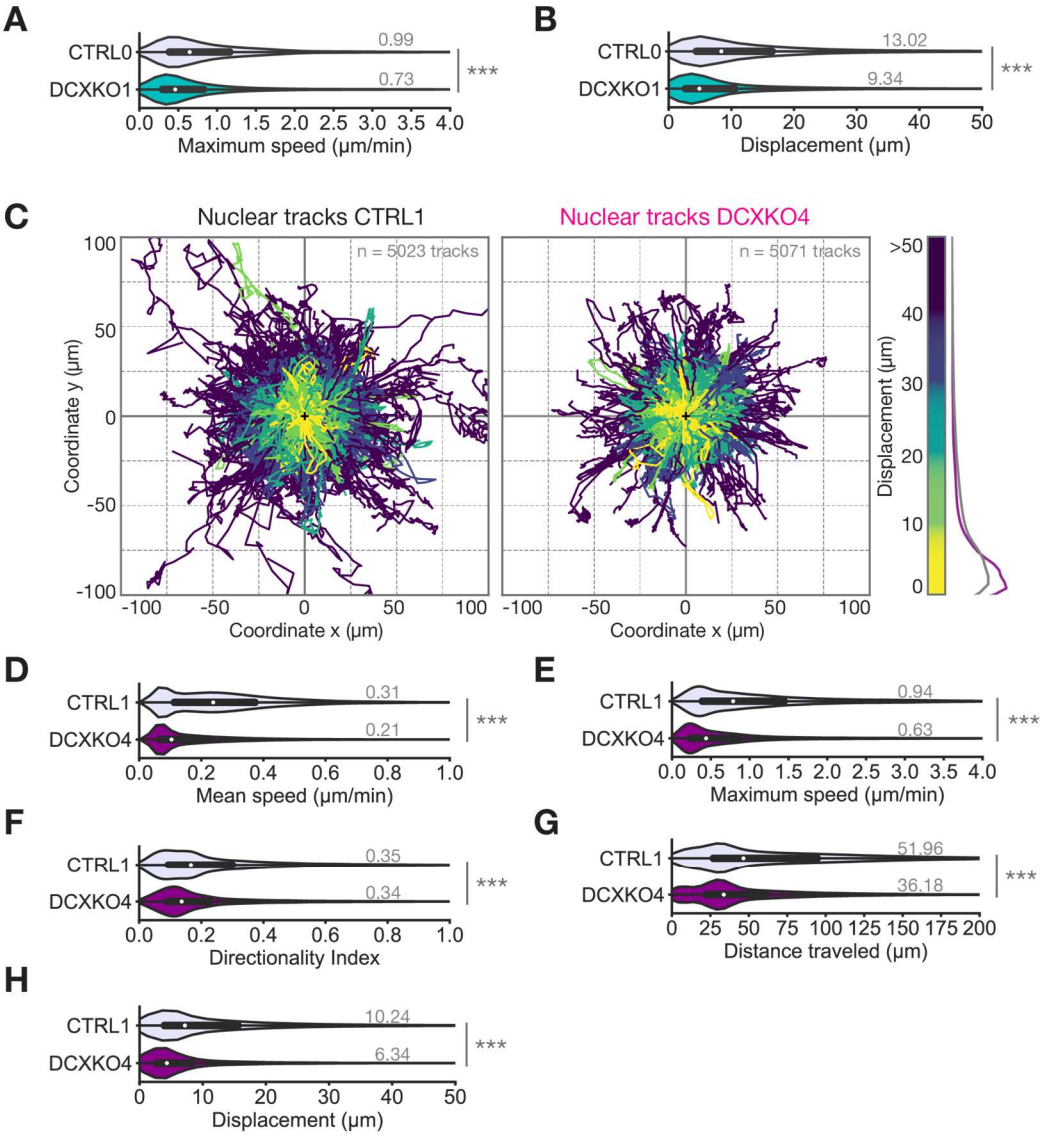

Figure S2: DCXKO1 and DCXKO4 neurons experience reduced migration speed and efficiency. (A) Distribution of maximum speed achieved by CTRL0 and DCXKO1 nuclei during the imaging period. **(B)** Distribution of displacement achieved by CTRL0 and DCXKO1 nuclei during the imaging period. For A-B, *n*=21826 control tracks and 6461 DCX-KO tracks from 3 paired experiments, tracks with less than 30min of imaging time were excluded from the dataset. Statistical analysis was performed using the Kruskal-Wallis non parametric H test: *** $p<0.001$. **(C)** Position plots showing a sample of trajectories extracted from CTRL1 (left) and DCXKO4 (right) nuclei tracking. All nuclei are considered to be at the same coordinates (0,0) at their first timepoint. Tracks are color-coded according to the displacement of the nucleus. Distribution of displacement for both genotypes are shown on the right end side of the panel. *n*=5023 and 5071 nuclei respectively for CTRL1 and DCXKO4. **(D)** Distribution of mean speed achieved by CTRL1 and DCXKO4 nuclei during the imaging period. **(E)** Distribution of maximum speed achieved by CTRL1 and DCXKO4 nuclei during the imaging period. **(F)** Distribution of directionality index for CTRL1 and DCXKO4 nuclei. Higher directionality index indicates more unidirectional movement. **(G)** Distribution of distance traveled by CTRL1 and DCXKO4 nuclei during the imaging period. H) Distribution of displacement achieved by CTRL1 and DCXKO4 nuclei during the imaging period. For D-H, *n*=49602 CTRL1B tracks and 29674 DCXKO4 tracks from 3 paired experiments, tracks with less than 30min of imaging time were excluded from the dataset. Statistical analysis was performed using the Kruskal-Wallis non parametric H test: *** $p<0.001$.

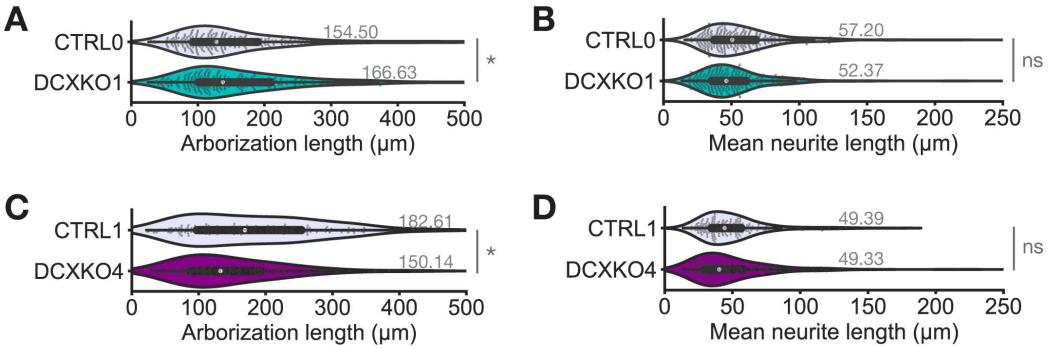

Figure S3: DCXKO1 and DCXKO4 have similar mean neurite length at DIV3. (A) Distribution of arborization length for fixed CTRL0 and DCXKO1 neurons used in the neurite counts. **(B)** Distribution of mean neurite length for fixed CTRL0 and DCXKO1 neurons used in the neurite counts. For A-B *n*=323 control and 351 DCXKO1 neurons from 3 experiments. Statistical analysis was performed using a Mann-Whitney U test: ns nonsignificant, * $p<0.05$. **(C)** Distribution of arborization length for fixed CTRL1 and DCXKO4 neurons used in the neurite counts. **(D)** Distribution of mean neurite length for fixed CTRL1 and DCXKO4 neurons used in the neurite counts. For C-D *n*=178 CTRL1 and 171 DCXKO4 neurons from 3 experiments. Statistical analysis was performed using a Mann-Whitney U test: ns nonsignificant, * $p<0.05$.

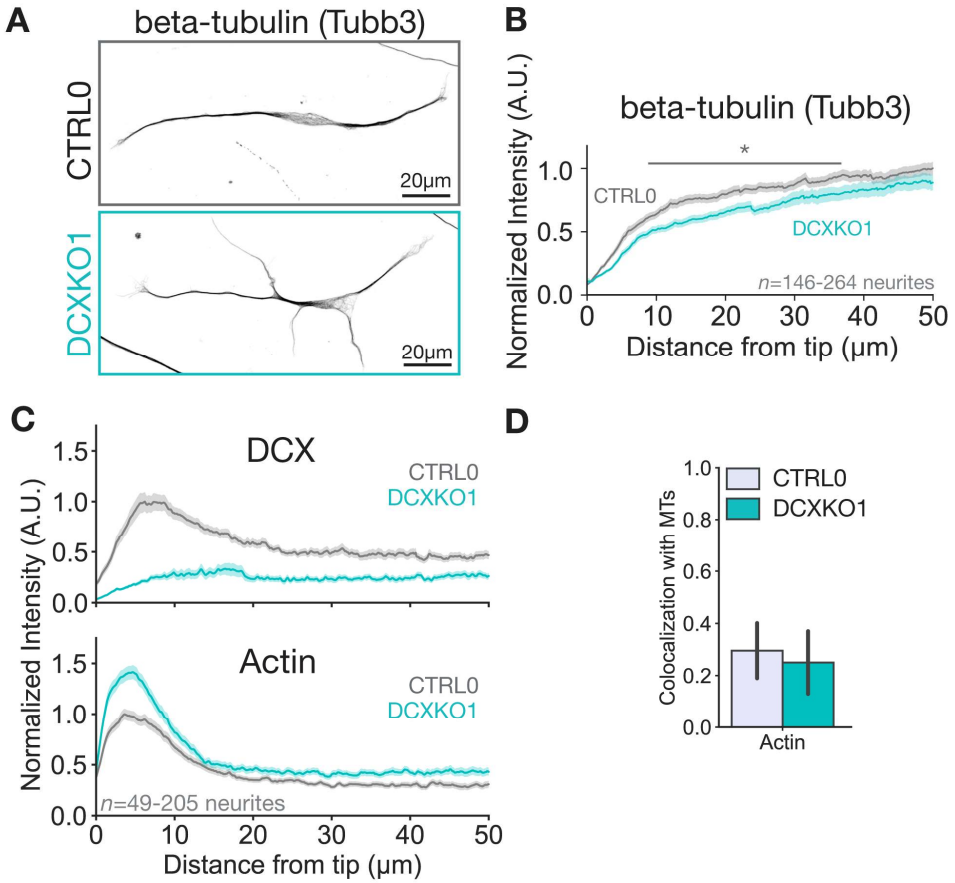

Figure S4: Modifications to tubulin and actin network in DCXKO neurons. (A) Representative immunostaining of CTRL0 and DCXKO1 neurons at DIV3 with an antibody against β3-Tubulin (Tubb3). **(B)** Mean β-Tubulin intensity profile +/- SEM. found in the distal tip of neurons for CTRL0 and DCXKO1. Images included in the analysis are from *n*=146 CTRL0 neurites and *n*=264 DCXKO1 neurites from 4 experiments. Statistical analysis was performed using the Mann-Whitney non parametric U test: ns nonsignificant. **(C)** Mean DCX and Actin intensity profiles +/- SEM. found in the distal tip of neurons for CTRL0 and DCXKO1. Images included in the analysis are from *n*=127-205 CTRL0 and *n*=49-145 DCXKO1 neurites for DCX and Actin respectively, from 2-3 independent experiments. **(D)** Percentage colocalization of Phalloidin with Tubb3 in the GC of neurons. *n*=65 CTRL0 GC and *n*=159 GC neurites from 2 experiments. Statistical analysis was performed using the Mann-Whitney non parametric U test: ns nonsignificant.

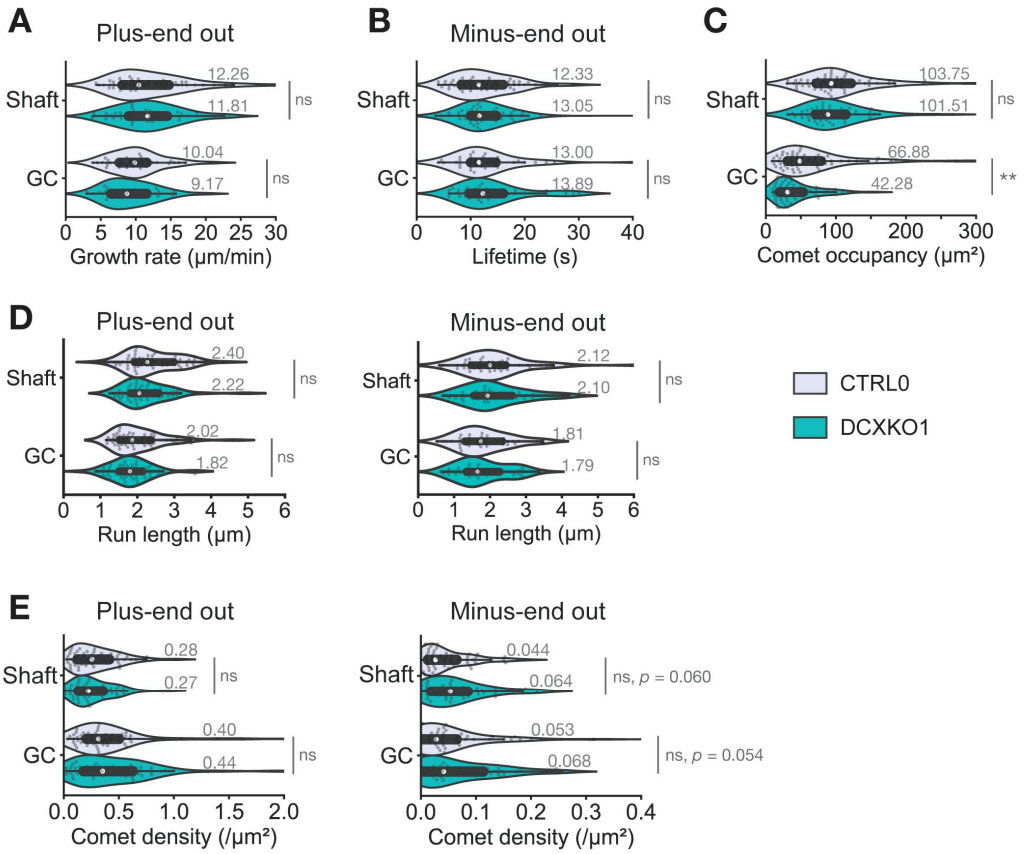

Figure S5: Microtubule dynamics are not different in DCXKO1 neurons. (A) Violin plot showing the distribution of growth rates for minus ends out comets in shaft or GC of CTRL0 and DCXKO1 neurons. **(B)** Violin plot showing the distribution of lifetimes for minus ends out comets in shaft or GC of CTRL0 and DCXKO1 neurons. **(C)** Violin plot showing the comet occupancy or area covered by EB3 comets during the imaging period. **(D)** Violin plot showing the distribution of run length for plus-end out and minus-end out comets in shaft or GC of CTRL0 and DCXKO1 neurons. **(E)** Violin plot showing the distribution of comet density for plus-end out and minus-end out comets in shaft or GC of CTRL0 and DCXKO1 neurons. Some plots were cut-off to better show the main population, but the maximum values for comet density and comet occupancy are 2.14 μm^{-1} and 438.10 μm^2 respectively. For A-E, n=63 control and n=63 DCXKO cells from 4 experiments. Statistical analysis was performed using the Mann-Whitney non parametric U test: ns nonsignificant, ** p<0.01.

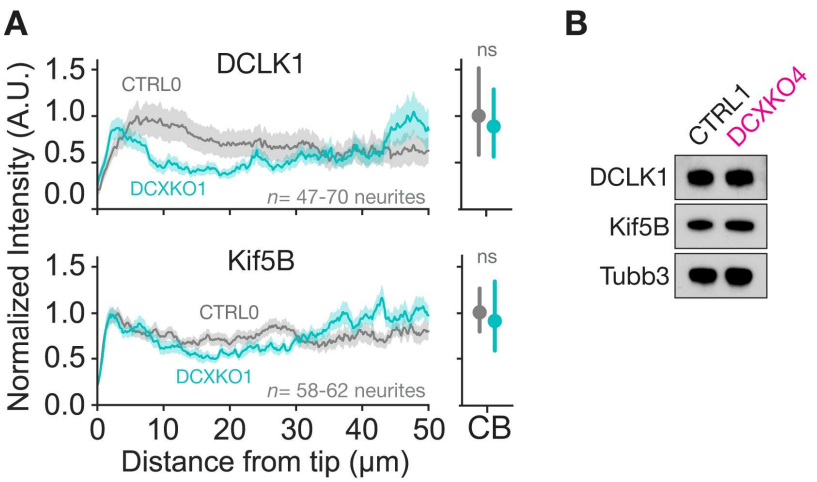

Figure S6: DCLK1 and Kif5B levels in DCX-KO neurons. (A) Mean intensity profiles +/- sem. of DCLK1 and Kif5B neurites distal ends and cell bodies (CB) +/- confidence interval for CTRL0 and DCXKO1 neurons. Images included in the analysis are from *n*=47-58 CTRL0 and *n*=70-62 DCXKO1 neurites for DCLK1 and Kif5B respectively from 4 experiments. Statistical analysis was performed using the Mann-Whitney non parametric U test: ns nonsignificant. **(B)** Immunoblot of CTRL1 and DCXKO4 neuron lysates at DIV3, with antibodies against DCLK1, Kif5B and Tubb3.

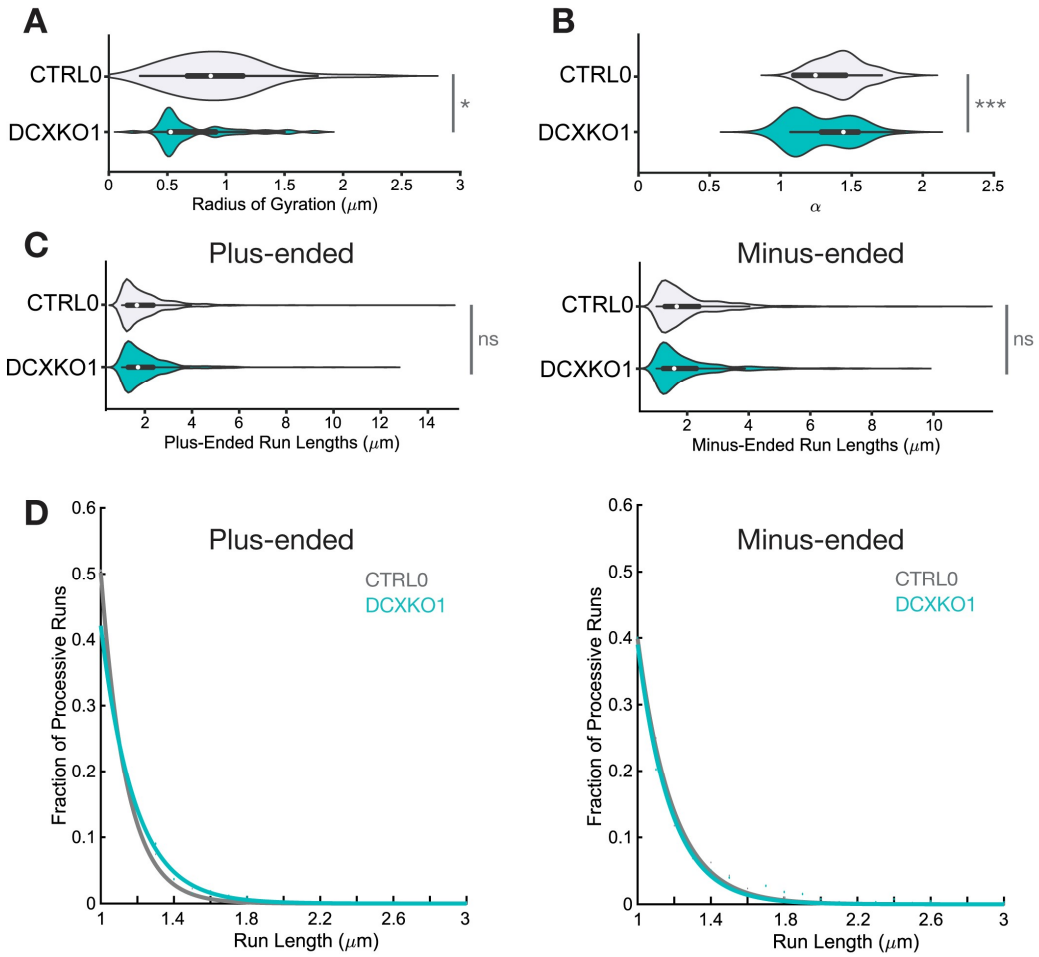

Figure S7: Alpha values and Rg for Lysosomes in DCXKO1. (A) Violin plot showing the radius of gyration of lysosomes in CTRL0 and DCXKO1 neurons. **(B)** Violin plot showing the alpha value of lysosomes in CTRL0 and DCXKO1 neurons. **(C)** Violin plot showing the distribution of plus-ended and minus-ended run length of lysosomes in CTRL0 and DCXKO1 neurons. **(D)** Fraction of plus-ended and minus-ended processive runs of lysosomes in CTRL0 and DCXKO1 neurons, depending on their run lengths. All trajectories (6082 for control and 3887 for DCXKO1) were obtained from *n*=41 control and 30 DCXKO1 neurons from 3 independent experiments. Statistical analysis was performed using the Student's t-test: ns nonsignificant, * $p<0.05$, *** $p<0.001$.

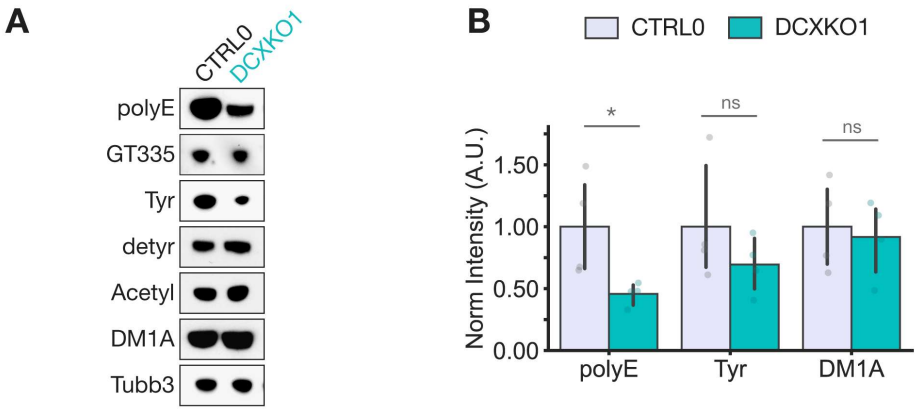

Figure S8: PTMs levels in DCXKO neurons. (A) Immunoblot showing the relative post-translational modifications levels in CTRL0 and DCXKO1 DIV3 neurons. **(B)** Immunoblot quantification showing polyglutamylation (polyE), tyrosination (Tyr) and α-tubulin (DM1A) levels normalized to tubulin-β3 (Tubb3) in CTRL0 and DCXKO1. *n*=4 CTRL0 and 4 DCXKO1 independent lysates. Statistical analysis was performed using the Student's t-test: ns nonsignificant, * $p<0.05$.

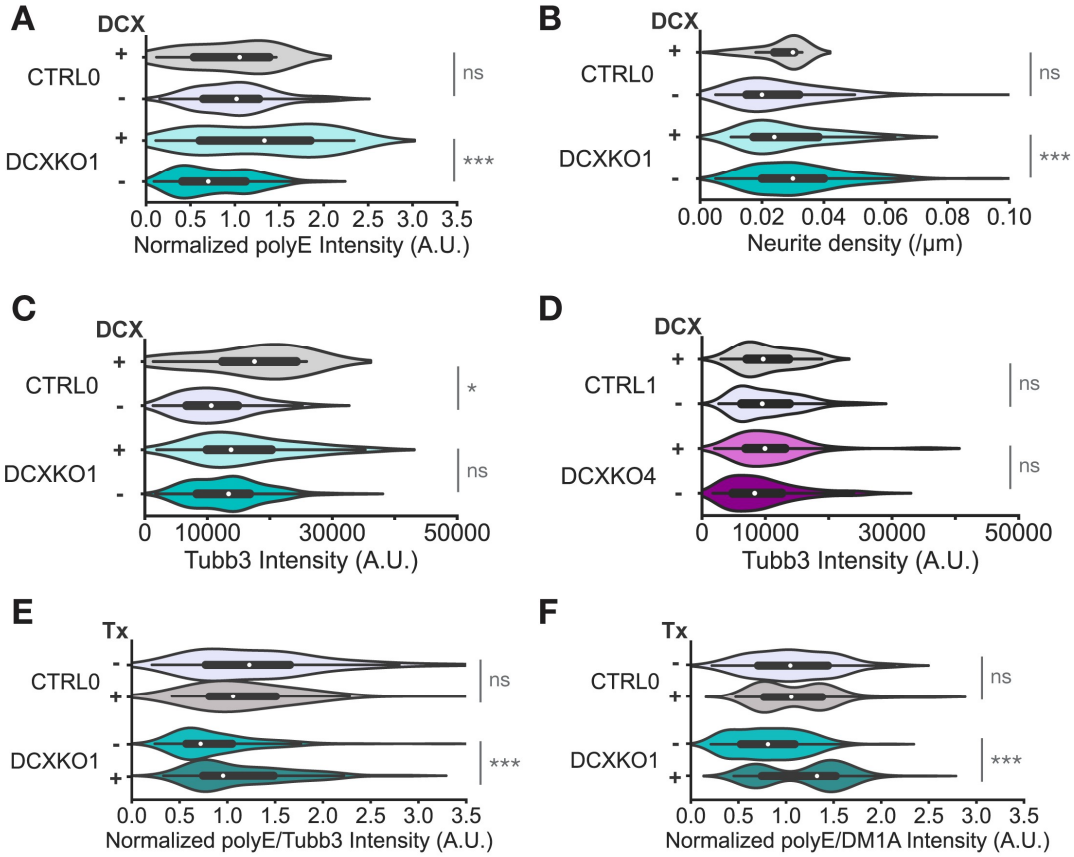

Figure S9: DCX reduces neurite numbers by increasing tubulin polyglutamylation levels. (A) Violin plots showing the polyglutamylation (polyE) intensity in CTRL0 and DCXKO1 DIV3 neurons with or without DCX-GFP electroporation, normalized to CTRL0. **(B)** Violin plot showing the neurite density in CTRL0 and DCXKO1 DIV3 neurons with or without DCX-GFP electroporation. This plot was cut-off to better show the main population, but the maximum value is 0.156 μm^{-1} for neurite density. **(C)** Violin plots showing the Tubb3 intensity in CTRL0 and DCXKO1 DIV3 neurons with or without DCX-GFP electroporation. For A-C, images included in the analysis are from *n*= 97 CTRL0, 11 CTRL0+DCX-GFP, 225 DCXKO1 and 38 DCXKO1+DCX-GFP neurons from 3 experiments. Statistical analysis was performed using the Mann-Whitney non parametric U test: ns nonsignificant, * $p<0.05$, *** $p<0.001$. **(D)** Violin plots showing the Tubb3 intensity in CTRL1 and DCXKO4 DIV3 neurons with or without DCX-GFP electroporation. Images included in the analysis are from n=178 CTRL1, 34 CTRL1+DCX-GFP, 171 DCXKO4 and 45 DCXKO4+DCX-GFP neurons from 3 experiments. Statistical analysis was performed using the Mann-Whitney non parametric U test: ns nonsignificant. **(E)** Violin plots showing the polyglutamylation (polyE) intensity in CTRL0 and DCXKO1 DIV3 neurons with or without Taxol treatment (Tx), normalized to Tubb3 intensity. **(F)** Violin plots showing the polyglutamylation (polyE) intensity in CTRL0 and DCXKO1 DIV3 neurons with or without Taxol treatment (Tx), normalized to DM1A intensity. For E-F, images included in the analysis are from *n*=84 CTRL0, 120 CTRL0+taxol, 172 DCXKO1 and 160 DCXKO1+taxol neurons from 2 experiments. Statistical analysis was performed using the Mann-Whitney non parametric U test: ns nonsignificant, * $p<0.05$, *** $p<0.001$. To note: as taxol treatment selectively enhances Tubb3 intensity, the effect of the treatment on polyE/Tubb3 seem lessen. However, taxol rescues polyglutamylation levels in DCXKO1 independently of the normalization method used.